PONTIFICIA UNIVERSIDAD CATÓLICA DE CHILE
FACULTAD DE FÍSICA
INSTITUTO DE FÍSICA

Search for long-lived dark photons decaying to hadronic lepton jets using the ATLAS detector

by

Richards González Andana

Thesis submitted to the Faculty of Physics of
Pontificia Universidad Católica de Chile,
in partial fulfillment of the requirements for
the academic Master's degree in Physics.

Supervisor : Prof. Marco Aurelio Díaz (PUC, Chile)
Committee : Prof. Francisca Garay(PUC, Chile)
Prof. Sebastián Olivares (UTA, Chile)

July 15^{th}, 2021
Santiago, Chile

To my mother Marcela, whose love and effort
have given me a life of opportunities

Abstract

Within the context of analyses looking for new particles in the ATLAS experiment at the Large Hadron Collider (LHC), a full event selection is designed to isolate simulated vector boson fusion (VBF) events where the Higgs boson decays to hadronic dark photon jet (hDPJ) signatures. Using this selection, a statistical significance of 4.2σ was obtained for a signal benchmark with a dark photon mass of $m_{\gamma_d} = 100$ MeV, decay length $c\tau = 15$ mm and decay $\gamma_d \to e^+e^-$. Additionally, a lifetime reweighting method is implemented to allow for exclusion limit estimations on $BR(H \to 2\gamma_d + X)$ as function of the dark photon proper decay length, given that all signal samples are generated with fixed γ_d lifetimes.

Declaration

I declare that this thesis is my own composition, and that the work presented here is my own except if explicitly stated otherwise in the document. Also, I declare that this work has not been published nor submitted, but used only in the context of the ATLAS Collaboration.

Richards González Andana
July, 2021

Acknowledgments

I would like to start thanking my mother, Marcela, for loving me and believing in me each second. All my love is yours, until time is no longer.

I would like to acknowledge Sebastián as my true advisor and as a true friend. Thank you for all the things you have taught me within and beyond particle physics. I wish nothing but the best for you and your family, and I hope we never loose touch.

I would also like to thank Andrés, who helped with many recommendations for this thesis. I am truly glad that you are living happily with your family, and I really hope to see you soon.

Finally but not least, I would like to thank Michael for his friendship and help in every matter. It is great to see you live a life you enjoy, and thanks for all the laughs!

Contents

Chapter 1

Introduction

The Standard Model (SM) describes the electroweak and strong interactions between all baryonic and leptonic matter in the Universe, but this matter only comprises about 5% of all the contents in the cosmos, the rest being denominated Dark Energy and Dark Matter (DM). One of the possible explanations for DM nature is that it is formed by Beyond Standard Model (BSM) particles, which are being extensively searched in different experiments. In recent years at the Large Hadron Collider (LHC), new strategies have appeared to search for new physics related to DM by studying exotic long-lived particles (LLP) that would leave distinguishable signatures in detectors like ATLAS. In this context, since the next data-taking period (Run-3) is expected to reach an integrated luminosity no more than two times the one achieved in the last period, many new LLP searches have appeared where signals of displaced vertices of only millimeters could easily be isolated from SM background.

Many BSM models predict LLPs that could be DM candidates, from which *dark/hidden sector* models stand out offering particularly interesting signatures in ATLAS. This type of models propose a dark sector that is very weakly coupled to known particles but can be mediated by SM particles as the Higgs boson. Usually, a new U(1) gauge symmetry could translate in an additional *dark photon* γ_d (and some dark fermions in a more sophisticated approach) that would be massive and unstable but long-lived, leaving a displaced vertex signature while decaying to SM particles visible for the detector in different possible final states.

Since these dark particles could be produced in Higgs decays, additional characterisation can be achieved using information related to a specific production mode. From those, this thesis focus on the Vector Boson Fusion (VBF) mode for the search of light dark photons with the ATLAS detector, that would decay to hadronic (jet-like) final states referred to as hadronic lepton jets (LJ). This is studied within the framework of the Falkowski–Ruderman–Volansky–Zupan (FRVZ) benchmark model [33; 34]. A full preselection and signal region definition is designed to isolate different VBF signal hypotheses from SM backgrounds in order to estimate exclusion limits in the future as function of the proper decay length of the putative dark photons.

Chapter 2 constitutes a succinct review of the SM and the Higgs boson. It contains an introduction to the elementary particles and forces leading to a description of the founding principles of the SM. Special attention is dedicated to the introduction of Spontaneous Symmetry Breaking (SSB) and the Higgs mechanism for the generation of gauge bosons masses, to then give way to a synthesis of the Higgs boson properties, including its production modes and decay channels. The chapter ends introducing the idea of exotic Higgs decays motivating displaced lepton jet searches in ATLAS, which will form the main subject of this work.

Chapter 3 treats the properties of the LHC and the ATLAS detector, as the experimental setup for all simulations and studies in this thesis. It includes details about the coordinate system used in all analyses by the collaboration, and about each sub-detector and its features regarding the reconstruction of the collisions.

Chapter 4 discusses the experimental signatures of hadronic dark photon jets produced in vector boson fusion events, constructing a whole set of preselection and selection cuts to isolate various signal hypotheses against different SM background processes. The chapter ends with an implementation of a lifetime reweighting algorithm for all signal samples, to allow for future estimations of exclusion limits as a function of the dark photon proper decay length.

Chapter 5 concludes the analysis and recapitulates the aspects of the search, while motivating future studies using this work as a starting point.

Chapter 2

The Standard Model, the Higgs boson and beyond

The Standard Model (SM) of particle physics holds the current description of nature at its most fundamental scale by postulating the existence of several elementary particles that represent matter and forces. Having special relativity and gauge symmetries at its core, most of its predictions at the subatomic scale have been empirically confirmed.

We start with a summary of the SM framework, focusing in features of the Higgs field as a cornerstone of BSM searches. Sect. 2.1 gives an elementary description of the SM particle content, followed by a review on symmetries and interactions in sect. 2.2, with special attention to the spontaneous breaking of the $SU(2)_L \times U(1)_Y$ symmetry and the Higgs Mechanism. Finally, an updated characterisation of the Higgs boson is given in sect. 2.3 together with a deeper look on dark/hidden sector models in sect. 2.4, focusing on the benchmark model used in this study.

2.1 Elementary particles and forces of nature

All the ordinary matter in the universe is formed by particles grouped in two categories: quarks and leptons. The former ones differentiating by existing only within the atomic nuclei, both groups are spin-1/2 particles whose free-propagation would be described by Dirac's equation; i.e., fermions. Every possible interaction between them occurs by exchanging gauge bosons, integer spin particles of scalar or vector nature that represent all forces in nature but gravity.

Electromagnetic interactions are mediated by *photons* γ which are massless and stable, while weak interactions are pictured as an exchange of $W^{\pm}$ and Z bosons, both kinds massive and unstable. The strong force, representing every interaction between quarks, is mediated by massless *gluons* that can also interact with each other.

Each fundamental interaction has a certain strength quantified by its coupling constant g (e.g. g_s for the strong force), that denotes the intensity with which a gauge boson couples to a fermion. The weak interaction is indeed the weakest of the three, being still much stronger than gravity.

A fermion may participate in a specific interaction if it exhibits the characteristic charge of that interaction. All particles with *electric charge* interact through photonic exchanges, with an intensity proportional to the amount of electric charge of the elementary particle. Quarks, while carrying fractional electric charge, also carry *colour charge* which comes in three different varieties. They interact via the strong force by exchanging gluons that also carry colour charge (each with one unit of colour and one of anti-colour), therefore being able to interact between themselves. Quarks form bound states (called baryons and mesons) that are globally colourless. In the case of weak interactions particles are characterised by an intrinsic weak isospin, but since electromagnetism and weak phenomena can be unified using the electroweak (EW) formalism, weak isospin and a new quantum number called *hypercharge* (that is only zero for gluons) are used to define electric charge following Gell-Mann-Nishijima's prescription [18]. Here, one of the most important features of EW interactions is the existence of the $W^{\pm}$ boson that, besides being the only gauge boson carrying electric charge, is the responsible for all flavour-changing interactions in the SM. It relates massive leptons with their respective neutrinos, and in strong interactions it can change any up-like quark to down-like and viceversa, where transition probability amplitudes are described by the Cabibbo-Kobayashi-Maskawa (CKM) matrix [7; 8].

Fermions are classified in three mass generations from lightest to heaviest, taking into account all the particles that form matter, whether stable or unstable. Heavier generations are not stable and quickly decay to stable particles from the first generation. In the case of leptons, massless neutrinos fall within the generations of their respective massive leptons. Here, even when the SM predicts them massless, oscillation experiments have proved that neutrino masses are indeed different from zero, where the flavour-mixing results from flavour eigenstates being linear combinations of mass eigenstates of the free-particle Hamiltonian (as in quark flavour-changing interactions).

The full particle content of the SM is depicted in figure 2.1, where antimatter should also be considered. Antiparticles, originally appearing as negative energy solutions to Dirac equation, are exactly the same as their matter partners but with opposite charge and magnetic moment relative to the spin.

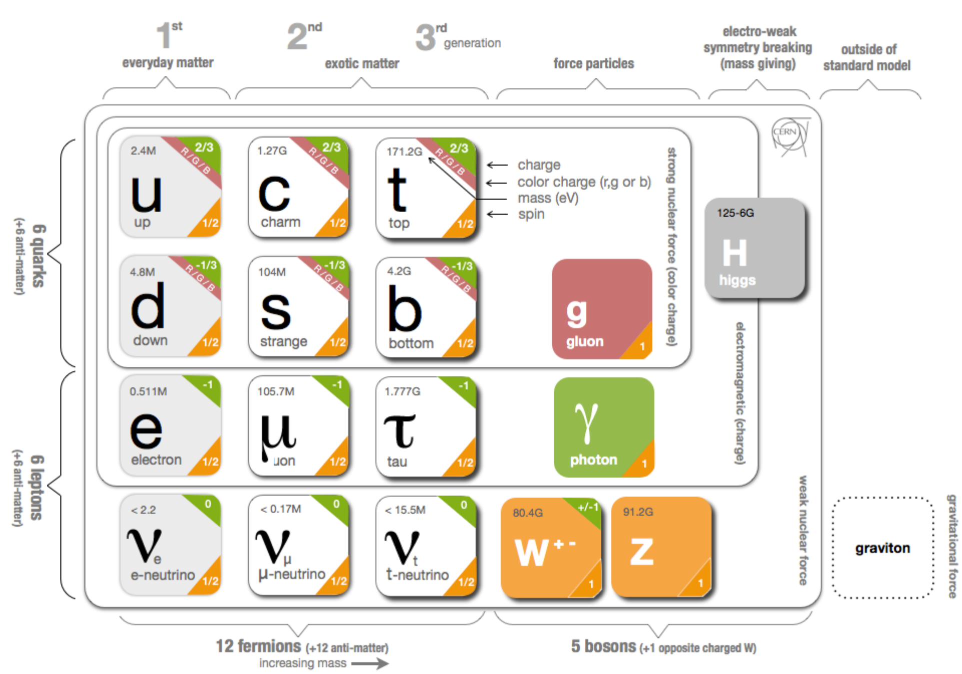

Figure 2.1: Table of the twelve elementary particles of matter (arranged in generations) together with the force-carriers of the EW and strong interactions, plus the Higgs boson [9].

The masses of all particles displayed arise from the interaction with the Higgs field, where mass generation is based in the asymmetry of the ground state of the vacuum where the EW symmetry is said to be spontaneously broken. This, in the context of the full model, is discussed in the following subsections.

2.2 Standard Model

2.2.1 Action and symmetry

From classical mechanics, the action S of a system is a functional of the generalised coordinates that corresponds to the integral of the Lagrangian $L = L(q_1(t), ..., q_N(t), \dot{q}_1(t), ..., \dot{q_N}(t), t)$ between two distinct instants. Having units of energy · time, it contains all the physical information of the system whose true evolution in time is given by the path for which the action is stationary under a first order perturbation. This variational principle is commonly known as of *least action*:

$$S = \int_{t_1}^{t_2} L \, dt \;\longrightarrow\; \delta S \equiv \frac{\delta S}{\delta[q_1...q_N](t)} = 0 \tag{2.1}$$

From here, we can show that a specific path is a stationary point of S if and only if

$$\frac{d}{dt}\frac{\partial L}{\partial \dot{q}_i} - \frac{\partial L}{\partial q_i} = 0, \quad i = 1, ..., N \tag{2.2}$$

where the solutions are the referred system's equations of motion.

This idea generalises to differentiable fields φ in space-time via a Lagrangian density $\mathcal{L} = \mathcal{L}(\varphi(x^\mu), \partial_\mu\varphi(x^\mu), x^\mu)$, now function of the field, its derivatives and the coordinates. The redefinition of the action follows as

$$S = \int \mathcal{L} \, d^4x \tag{2.3}$$

where it being invariant under a first order field transformation equals to satisfying Euler-

Lagrange equations in their field formulation:

$$\partial_\mu \frac{\partial \mathcal{L}}{\partial(\partial_\mu \varphi)} - \frac{\partial \mathcal{L}}{\partial \varphi} = 0$$

For each transformation leaving the action invariant it is said that the action is symmetric under that certain transformation, stating that for every differentiable symmetry of the action there is a conserved current density j^μ, where the conservation law takes the form of a continuity equation (as usual):

$$\partial_\mu j^\mu = 0 \tag{2.4}$$

With this in mind, we can continue to describe the construction of the SM framework from the group of symmetries of nature to its full Lagrangian description.

2.2.2 Poincaré group

Being the SM a relativistic quantum field theory, invariance of physical laws under Poincaré transformations is one the pillars of modern particle physics. This reflects the redefinition of simultaneity as the speed of light must be the same in every inertial frame.

Including Lorentz transformations (boosts and spatial rotations) and space-time translations, the Poincaré group has ten generators (six for the former and four for the latter) and its algebra is given by

$$[P_\mu, P_\nu] = 0 \tag{2.5}$$

$$[M_{\mu\nu}, M_{\alpha\beta}] = i(g_{\mu\alpha}M_{\nu\beta} - g_{\mu\beta}M_{\nu\alpha} - g_{\nu\alpha}M_{\mu\beta} + g_{\nu\beta}M_{\mu\alpha}) \tag{2.6}$$

$$[M_{\mu\nu}, P_\alpha] = i(g_{\mu\alpha}P_\nu - g_{\nu\alpha}P_\mu) \tag{2.7}$$

where M generates Lorentz transformations, P generates translations and g is the metric tensor. In this way, a particle state falls into an irreducible representation of the group and quantum field theories are realisations of this algebra, with Lagrangians that must be invariant under the transformation rules for each kind of field (classified by spin).

2.2.3 Gauge groups

The full Lagrangian of the SM is constructed in such a way that it must be invariant under certain local transformations denominated *gauge transformations*. These are related to redundant degrees of freedom of the Lagrangian, and form continuous transformation groups (i.e. Lie groups with their associated algebra) that are usually referred to as gauge symmetry groups.

The overall gauge group of the SM corresponds to

$$SU(3)_C \times SU(2)_L \times U(1)_Y$$

(with all groups of unitary transformations and, in the case of $SU(2)$ and $SU(3)$, with determinant equals to 1) where C stands for colour charge, L for the left-handed fermions, and Y for hypercharge (defined as $Y = 2(Q - I_3)$, with Q the electric charge and I_3 the third isospin component). Therefore, the most general gauge transformation for a Dirac spinor ψ is given by

$$\psi \to \psi' = e^{-ig_s \gamma^a(x)\lambda^a/2} e^{-ig_w \beta^k(x)\sigma^k/2} e^{-ig_y \alpha(x)Y/2} \psi \tag{2.8}$$

where g_s, g_w and g_y are the strong, weak and QED coupling constants, respectively; and γ, β and α are local space-time dependent phases. From right to left, the first exponential corresponds to a U(1) transformation generated by Y, which is a number conventionally assigned to each particle. The second exponential is a SU(2) transformation whose generators $\vec{T}$ can be expressed in terms of the Pauli matrices as $\vec{T} = \vec{\sigma}/2$ and whose algebra is given by $[T^i, T^j] = i\epsilon^{ijk}T^k$ ($i, j, k = 1$ to 3 and ϵ the Levi-Civita tensor), which can be deduced from commutation relations for σ matrices. Finally, the third exponential corresponds to a SU(3) transformation generated by $\vec{T} = \vec{\lambda}/2$, where λ^a ($a = 1, ..., 8$) are the Gell-Mann matrices. SU(3) generators must fulfill $[T^a, T^b] = if^{abc}T^c$, with f^{abc} the group structure constants.

Since the main feature of gauge transformations is that they are local, one additional gauge field per group generator has to be added to the derivative to render the Lagrangian gauge invariant via minimal substitution. This new derivative corresponds to the covariant derivative that, for gauge fields transforming as

$$G^a_\mu \to G^{a\prime}_\mu = G^a_\mu - \partial_\mu \gamma^a - g_s f^{abc} \gamma^b G^c_\mu \tag{2.9}$$

$$W^i_\mu \to W^{i\prime}_\mu = W^i_\mu - \partial_\mu \beta^i - g_w \epsilon^{ijk} \beta^j W^k_\mu \tag{2.10}$$

$$B_\mu \to B'_\mu = B_\mu - \partial_\mu \alpha \tag{2.11}$$

is given by:

$$D_\mu = \partial_\mu + i g_s G^a_\mu \frac{\lambda^a}{2} + i g_w W^i_\mu \frac{\sigma^i}{2} + i g_y B_\mu \frac{Y}{2} \tag{2.12}$$

Kinetic terms must be added to account for the free propagation of spin-1 fields introduced. For this, field strength tensors are defined like

$$G^a_{\mu\nu} = \partial_\mu G^a_\nu - \partial_\nu G^a_\mu - g_s f^{abc} G^b_\mu G^c_\nu \tag{2.13}$$

$$W^i_{\mu\nu} = \partial_\mu W^i_\nu - \partial_\nu W^i_\mu - g_w \epsilon^{ijk} W^j_\mu W^k_\nu \tag{2.14}$$

$$B_{\mu\nu} = \partial_\mu B_\nu - \partial_\nu B_\mu \tag{2.15}$$

and the gauge invariant kinetic terms of the fields are included to the SM Lagrangian:

$$\mathcal{L}^{kin}_{gauge} = -\frac{1}{4} G^a_{\mu\nu} G^{\mu\nu}_a - \frac{1}{4} W^i_{\mu\nu} W^{\mu\nu}_i - \frac{1}{4} B_{\mu\nu} B^{\mu\nu} \tag{2.16}$$

2.2.4 Discrete symmetries

Even if we have only discussed groups of continuous symmetries up to this point, discrete transformations that leave quantum systems unchanged are also present in nature.

When a system or process occurring in nature suffers an inversion that turns it into its mirror image and the resulting process still occurs physically, the process is said to be invariant under *parity* transformations (represented by the parity operator $\hat{P}$). As a projection operator it has eigenvalues ± 1 and applying it twice returns the system to its original state ($P^2 = I$), which shows that parity is a multiplicative quantum number.In our universe, only the electromagnetic and strong interactions are observed to be invariant under parity. The weak force, by its side, is said to maximally violate parity. This can be observed, for example, in the complete absence of right handed neutrinos in nature.

Another discrete symmetry of nature can be inferred from classical electrodynamics. Since it is evident that the whole theory would come out the same if we decided to change the sign of all electric charges, it is said to be invariant under *charge conjugation*. Charge conjugation operator $\hat{C}$ converts each particle into its antiparticle (i.e., $\hat{C}\,|\psi\rangle = |\bar{\psi}\rangle$) and applying it twice will return the system to its original state. Thus, charge conjugation eigenvalues are ± 1 and only particles that are their own antiparticle may be eigenstates. At this point it is important to note that, even though $\hat{P}$ and $\hat{C}$ are not absolute symmetries of nature, it is valid to wonder if the mixed CP symmetry could still be an option. Nevertheless, it has been observed to be minimally violated in kaons and neutral B mesons decays, and it is thought to be responsible of the matter-antimatter asymmetry in the universe.

Finally and equally important, *time reversal* operations $\hat{T}$ are also discrete transformations that, by themselves, are not exact symmetries of nature. Indeed, there are compelling reasons to assert that it should not be an absolute symmetry, in direct relation to the CPT theorem. As one of the most important results of QFT, we know that the combined operation of charge conjugation, parity and time reversal must be an exact symmetry of any interaction in nature; implying, for example, that every particle must have the exact mass and lifetime than its antiparticle. This establishes the theorem in firm theoretical and empirical ground, but it does not stop scientists from testing it in contemporary experiments within high energy physics.

2.2.5 Particles and representations

As previously mentioned, all particles in the SM can be categorised in two main groups: fermions and bosons.

Fermions, including quarks and leptons, come in two chiralities[1]: left and right-handed. The only particles that do not follow this prescription are neutrinos, since no right-handed neutrino or left-handed antineutrino has ever been observed. All left-handed fermions transform as doublets under $SU(2)$ transformations, while for right-handed fermions a distinction has to be made; right-handed leptons are singlets under both $SU(2)$ and $SU(3)$, but right-handed quarks are singlets only under $SU(2)$, and triplets under $SU(3)$. Left-handed quarks at last, they also transform as triplets under $SU(3)$.
Each one of the three fermion generations behaves equally under a transformation of a given group. In this manner, it is convenient to group leptons denoting them by $\ell_{iL,R}$, and quarks by $u_{iL,R}$ (for *up*, *charm* and *top*) and $d_{iL,R}$ (for *down*, *strange* and *bottom*), where $i = 1, 2, 3$ to account for each flavour.

Regarding mediator particles, the eight $SU(3)$ fields introduced in the covariant derivative corresponds to gluons, and the four fields of $SU(2)$ and $U(1)$ will mix to give rise to vector bosons. The Higgs boson, on its own, can be thought as being contained in a $SU(2)$ scalar doublet representing the Higgs field, and his role in the rise of gauge bosons and fermion masses will be treated in section 2.2.7.

2.2.6 Strong interactions and Quantum Chromodynamics (QCD)

The C subscript in $SU(3)_C$ refers to colour space as the phase space of strong interactions. This corresponds to the gauge symmetry of Quantum Chromodynamics [10; 11; 12; 13], and it implies the conservation of colour charge. The colour wavefunction basis is defined with red r, green g and blue b, where all quarks carry one unit of colour or anticolour and gluons carry one of each kind. This last aspect is special of QCD.
With the eight $SU(3)$ algebra generators constructed from Gell-Mann matrices λ^a, the local phase transformation represents a different rotation in colour space at every point in space-time, and one new gauge field for each group generator must be added to the derivative to account for this. These are the eight fields G^a that correspond to gluons in

[1] *Chirality* is the homologous of helicity for massless particles and is defined, roughly, by the action of γ^5 as a chiral projection operator. The distinction is made since helicity is not Lorentz invariant for massive particles.

QCD.

Despite the evidence for the existence of quarks (e.g., from deep inelastic scattering), no free quark has ever been observed. In the SM, this topic is addressed through the *colour confinement* hypothesis, where particles exhibiting colour charge cannot propagate freely but are instead confined to colour singlets. As a consequence, all quarks in nature form colourless bound states known as hadrons, either as mesons ($q\bar{q}$) or baryons (qqq and $\bar{q}\bar{q}\bar{q}$) [14; 15]. This effect is believed to originate from gluon self-interactions happening because gluons also carry colour charge. In the same line, regarding the non-abelian nature of QCD, gluon self-interactions translate in corrections to the gluonic propagator due to new gluon loops that cause the strong coupling constant to decrease as function of the energy scale, therefore allowing perturbative calculations in high-energy regimes (which is known as QCD's *asymptotic freedom* [12; 13]). At lower energies though, the interaction becomes stronger and bound states form.

Colour confinement has direct consequences, for example, in hadron colliders. Since quarks are confined within protons before a collision, the exact amount of energy consumed in each reaction at the interaction point is unknown. For an accurate description of hard inelastic collisions, Parton Distribution Functions (PDF) in QCD collinear factorisation [16] are used to quantify the probability of finding certain partons in an hadron, at some energy scale Q^2, as a function of the fraction x of the hadron's momentum carried by the parton. PDFs, although at different scale Q^2, are also needed to accurately describe hadronic processes after a collision. After partonic showers result in the formation of many hadrons and leptons, off-shell partons with virtualities close to the chosen cut-off scale remain to be modelled, now in a regime where non-perturbative effects are important. From these effects the most relevant is hadronisation, where a boosted cone of particles forms starting with a single quark or gluon. These processes, while yet not fully comprehended by QCD, can be approximated using parameterisation models of great importance for event generators based in Monte Carlo simulation. Here, many algorithms are used to incorporate into the description phenomena like initial and final state radiation (ISR/FSR), jet matching/merging at different multiplicities, and next-to-leading order (NLO) effects.

2.2.7 EW theory, Spontaneous Symmetry Breaking and the Higgs mechanism

The modern realisation of electroweak interactions originated in the sixties from the work of Glashow, Weinberg and Salam [1; 2; 17], earning them the 1979 Nobel Prize in Physics. Glashow started in 1961 by proposing the $SU(2) \times U(1)$ symmetry group with the appearance of an additional gauge boson, named Z^0. The new conserved charge of the interactions corresponded to weak hypercharge, defined (in the same way specified in sect. 2.2.3) from electric charge and weak isospin following Gell-Mann−Nishijima's prescription [18].

Due to observations of parity-violating weak interactions in 1956's experiment by Chien-Shiung Wu [19], theoretical efforts at the time were invested in constructing a framework that would describe such phenomenon. From QED, it is known that the most general Lorentz-invariant form for a fermion-boson interaction is given by a linear combination of bilinear covariants, with the current transforming as a vector. Indeed, if this is restricted to the exchange of a spin-1 (i.e., vector) boson, the most general form of the interaction includes also axial vector currents, looking like $j^\mu_A = \bar{u}(p')\gamma^\mu\gamma^5\bar{u}(p)$. This results in the so-called V-A structure of weak interactions, and it provides a mechanism to explain the observed violation of parity in the weak force. In fact, the V-A nature of the vertex factor is visible in the charged current,

$$j^\mu = \frac{g_w}{\sqrt{2}}\bar{u}(p')\frac{1}{2}\gamma^\mu(1-\gamma^5)u(p) \tag{2.17}$$

where the left-chiral projection operator $\frac{1}{2}(1-\gamma^5)$ can be recognised. This reveal to us that *only* left-handed chiral particles and right-handed chiral antiparticles can participate in charged weak interactions, and allows us to understand that the maximally different coupling of the $W^\pm$ boson to left-handed and right-handed chiral states is the origin of parity violation. This is also reflected in the fact that gauge transformations for right-handed particles are generated by hypercharge only. Thus, the actual gauge group for electroweak interactions is given by $SU(2)_L \times U(1)_Y$, and the W^i_μ and B_μ gauge fields are introduced in the derivative by minimal substitution, as specified in sect. 2.2.3. The electroweak Lagrangian, then, corresponds to:

$$\mathcal{L}_{EW} = \mathcal{L}_{ferm} + \mathcal{L}_{gauge} \tag{2.18}$$

$$\mathcal{L}_{EW} = \sum_{ferm} i\bar{\psi}\not{D}\psi - \frac{1}{4}W^i_{\mu\nu}W_i^{\mu\nu} - \frac{1}{4}B_{\mu\nu}B^{\mu\nu} \tag{2.19}$$

Despite the success of the EW theory at unifying electromagnetism and weak interactions under a single theoretical framework, it was not yet complete since it did not predict gauge bosons masses and simply adding individual mass terms would render the theory not gauge invariant. To solve this, an alternative origin to gauge boson masses appeared during the first years of the 1960 decade, based on *spontaneous symmetry breaking* (SSB).
Starting by introducing a $SU(2)$ doublet complex scalar field Φ of the form

$$\Phi = \frac{1}{\sqrt{2}}\begin{pmatrix}\phi_1 + i\phi_2 \\ \phi_3 + i\phi_4\end{pmatrix} \tag{2.20}$$

where ϕ_i are real scalar fields, the Lagrangian density corresponds to

$$\mathcal{L}_{scalar} = (D_\mu\Phi)^\dagger(D^\mu\Phi) - V(\Phi^\dagger\Phi) \tag{2.21}$$

The potential V that will spontaneously break the $SU(2)_L \times U(1)_Y$ symmetry is given by

$$V(\Phi^\dagger\Phi) = \mu^2\Phi^\dagger\Phi + \lambda(\Phi^\dagger\Phi)^2 \tag{2.22}$$

with $\mu^2 < 0$ (i.e., complex), displaying a minimum when $\phi_1^2 + \phi_2^2 + \phi_3^2 + \phi_4^2 = -\mu^2/2\lambda$. One can choose a vacuum state that satisfies

$$\langle 0|\,\Phi\,|0\rangle = \frac{1}{\sqrt{2}}\begin{pmatrix}0 \\ v\end{pmatrix} \tag{2.23}$$

where $v = \sqrt{-\mu^2/\lambda}$ is the vacuum expectation value (or *vev*) of the field. At this point it becomes clear that, even when the field Lagrangian remains invariant under $SU(2)_L \times U(1)_Y$, the vacuum state is not since any $SU(2)$ rotation would change it; meaning that the symmetry has been spontaneously broken.

Now, the Goldstone theorem [3] declares that for each broken generator ('degree of freedom') of a continuous symmetry a massless scalar particle (called Nambu-Goldstone boson) appears, which in this case is equal to three due to the three $SU(2)$ generators. Taking advantage of the gauge freedom, Goldstone bosons traduce in the longitudinal polarisation state of gauge bosons [4; 5; 6]. Writing the scalar doublet in the unitary gauge with a small real scalar perturbation h around the vacuum

$$\Phi = \frac{1}{\sqrt{2}} \begin{pmatrix} 0 \\ v+h \end{pmatrix} \tag{2.24}$$

we can foresee that the kinetic term of the scalar field will contain terms corresponding to gauge bosons masses. The derivative of the field is given by (choosing $Y = 1$ for the doublet)

$$D_\mu \Phi = (\partial_\mu + i\frac{g_y}{2} B_\mu + i\frac{g_w}{2} W_\mu^i \sigma^i) \begin{pmatrix} 0 \\ \frac{v+h}{\sqrt{2}} \end{pmatrix} \tag{2.25}$$

such that, defining

$$W_\mu^\pm = \frac{1}{\sqrt{2}}(W_\mu^1 \mp i W_\mu^2) \quad \text{and} \quad W_\mu = W_\mu^i \sigma^i = \begin{pmatrix} W_\mu^3 & \sqrt{2} W_\mu^+ \\ \sqrt{2} W_\mu^- & -W_\mu^3 \end{pmatrix} \tag{2.26}$$

we can rewrite as:

$$D_\mu \Phi = \begin{pmatrix} 0 \\ \frac{\partial_\mu h}{\sqrt{2}} \end{pmatrix} + i\frac{g_y}{2} B_\mu \begin{pmatrix} 0 \\ \frac{v+h}{\sqrt{2}} \end{pmatrix} + i\frac{g_w}{2} \begin{pmatrix} W_\mu^+ (v+h) \\ -W_\mu^3 (\frac{v+h}{\sqrt{2}}) \end{pmatrix} \tag{2.27}$$

From this expression the kinetic term renders:

$$(D_\mu \Phi)^\dagger (D^\mu \Phi) = \frac{1}{2} \partial_\mu h \partial^\mu h + \frac{1}{2} g_w^2 W_\mu^- W^{\mu +} \Big(\frac{v+h}{\sqrt{2}}\Big)^2 \tag{2.28}$$

$$+ \Big(\frac{1}{4} g_y^2 B_\mu B^\mu - \frac{1}{2} g_y g_w B_\mu W^{\mu 3} + \frac{1}{4} g_w^2 W_\mu^3 W^{\mu 3}\Big) \Big(\frac{v+h}{\sqrt{2}}\Big)^2 \tag{2.29}$$

The mass term for the charged W bosons, mixture of W^1 and W^2, arise from the last term in eq. 2.28:

$$m_W^2 = \frac{v^2}{4} g_w^2 \tag{2.30}$$

The whole term in eq. 2.29 suggests that physical bosons are a mixture of the B_μ and W_μ^3 gauge fields. To diagonalise the mass matrix, a redefinition is introduced

$$A_\mu = \cos\theta_W B_\mu + \sin\theta_W W_\mu^3 \tag{2.31}$$

$$Z_\mu = -\sin\theta_W B_\mu + \cos\theta_W W_\mu^3 \tag{2.32}$$

where A_μ and Z_μ correspond to the photon and the neutral Z boson, respectively, and θ_W is Weinberg's angle defined as:

$$\tan\theta_W = \frac{g_y}{g_w} \tag{2.33}$$

With this, rewriting the mass term in the Lagrangian yields

$$\mathcal{L}_{mass} = \frac{v^2}{8}(g_y^2 + g_w^2) Z_\mu Z^\mu \ (+\, 0 \cdot A_\mu A^\mu) \tag{2.34}$$

where the masses are, visibly:

$$m_Z^2 = \frac{v^2}{4}(g_y^2 + g_w^2) \quad \text{and} \quad m_A = 0 \tag{2.35}$$

This whole mechanism for the generation of gauge bosons masses through electroweak symmetry breaking receives the name of *Higgs mechanism*. The mass of the Higgs boson h itself comes from its self-interaction and is contained in the potential term $V(\Phi^\dagger\Phi)$. The mass (and dynamics) of the rest of the SM particles is discussed below, in sect. 2.2.8.

2.2.8 Fermionic content

All fermions in the SM are arranged in left-handed doublets and right-handed singlets under $SU(2)_L$. Sticking to the notation introduced in sect. 2.2.5, the fermionic kinetic terms are built promoting partial to covariant derivatives now containing the physical gauge fields for the different forces

$$\mathcal{L}_{ferm}^{kin} = i\sum_{i=1}^{3}\big(\bar{Q}_{iL}\bar{\sigma}^{\mu}D_{\mu}Q_{iL} + \bar{u}_{iR}\sigma^{\mu}D_{\mu}u_{iR} + \bar{d}_{iR}\sigma^{\mu}D_{\mu}d_{iR} \tag{2.36}$$

$$+ \bar{\ell}_{iL}\bar{\sigma}^{\mu}D_{\mu}\ell_{iL} + \bar{e}_{iR}\sigma^{\mu}D_{\mu}e_{iR}\big) \tag{2.37}$$

where $\sigma^{\mu} = (I, \vec{\sigma})$. From here, fermion couplings to gauge bosons can be obtained directly by expanding the covariant derivative. Regarding mass, fermion masses are generated in the SM by means of Yukawa type interactions of the form

$$-\mathcal{L}_{Yuk} = Y_{ij}^{\ell}\bar{\ell}_{iL}\Phi e_{jR} + Y_{ij}^{u}\bar{Q}_{iL}\tilde{\Phi}u_{jR} + Y_{ij}^{d}\bar{Q}_{iL}\Phi d_{jR} + h.c. \tag{2.38}$$

where $\tilde{\Phi} = i\sigma_2\Phi^*$ is defined to ensure massive u quarks. The matrices $Y^{\ell,u,d}$ correspond to lepton, up and down-type dimensionless Yukawa couplings. To be precise, fermion masses arise after SSB and are given by:

$$-\mathcal{L}_{Yuk}^{mass} = \frac{v}{\sqrt{2}}\big(Y_{ij}^{\ell}\bar{e}_{iL}e_{jR} + Y_{ij}^{u}\bar{u}_{iL}u_{jR} + Y_{ij}^{d}\bar{d}_{iL}d_{jR}\big) + h.c. \tag{2.39}$$

Having both the kinematic and masses of gauge bosons and fermions, the main features of the SM have been visited. The following section provides a brief description of the Higgs boson and its measured properties.

2.3 The Higgs boson

The Higgs particle, as mentioned in sect. 2.2.7, corresponds to an excitation of the Higgs field (i.e., an excited state over the vacuum ground state) and allows SM particles to acquire mass. Its existence was first inferred from the work of three different groups in the middle sixties [4; 5; 6], and later confirmed in 2012 by the ATLAS [20] and CMS [21] experiments at CERN's Large Hadron Collider (LHC) in Geneva. For this, Peter Higgs and François Englert were awarded the 2013 Nobel Prize in Physics.

2.3.1 Properties

The Higgs boson discovery in 2012 led to numerous studies aiming to study its properties precisely in order to confirm if it is, indeed, the SM boson theorised in the past century.

The first measured feature was the mass since it is equal to the invariant mass of its decay products, being the studied parameter of interest to fit the observed data distribution at its discovery. With a combined measurement of $m_H = 125.09 \pm 0.21(\text{stat.}) \pm 0.11(\text{syst.})$ GeV between CMS and ATLAS [22], the boson mass was observed to be within SM expectations in relation to top quark and gauge bosons masses. Regarding spin and parity observables, it is a CP-even scalar boson (parity eigenvalue +1 and spin-0). Different CP and spin hypothesis were out years ago by measurements of angular distributions and spin correlations in Higgs decays to a pair of vector bosons [23].

Many studies have been performed about Higgs boson couplings to the rest of the SM particles [24]. We can estimate them directly from the Lagrangian terms containing the desired interactions (see, for example, eq. 2.40) and then compare with measurements of production and decay modes. This directly restricts the precision level with which the Higgs couplings can be studied since not all predicted Higgs interactions have been observed.

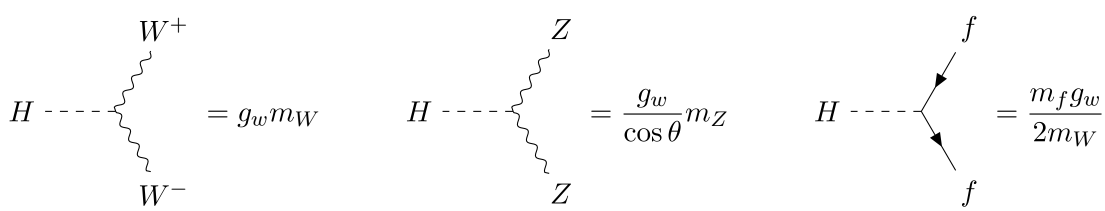

(2.40)

2.3.2 Production modes

The Higgs may be produced in several reactions depending on the nature of the collider, where for the LHC, bunches of protons collide head-to-head favouring deeply inelastic partonic scattering as means to maximise the number of produced particles. In this scenario, most of Higgs events come from gluon-gluon fusion (ggF) processes, where the scalar is created via quark loops. The following production mode in cross-section magnitude corresponds to vector boson fusion (VBF) processes, that characteristically show a pair of boosted quarks in the detected final state. The Feynman diagrams for these two production modes are shown in fig. 2.2.

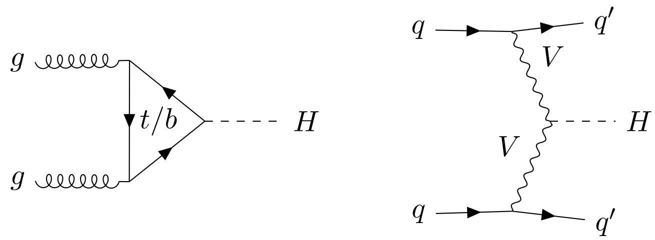

Figure 2.2: Gluon-gluon fusion (left) and vector boson fusion (right) leading-order (LO) diagrams. For ggF, top and bottom quarks are explicitly highlighted in the loop since together are the main contribution to the amplitude.

The following Higgs production modes with a lower cross-section at the LHC correspond to VH (WH,ZH) and $t\bar{t}H/b\bar{b}H$ production. The full relative contribution of each production mode is shown in figure 2.3.

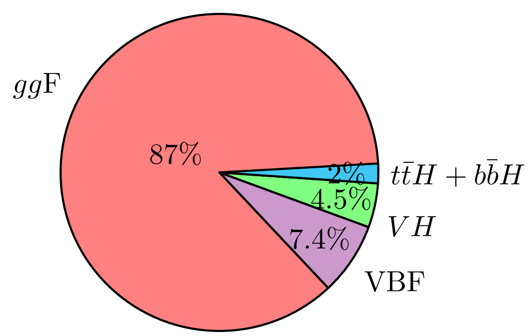

Figure 2.3: Proportional contribution from each production mode considering pp collisions at the LHC at a centre-of-mass energy of $\sqrt{s} = 13$ TeV and a Higgs mass of $m_H = 125$ GeV.

2.3.3 Decay channels and width

As an unstable particle, the Higgs boson decays and the transition rate Γ_i to each final state is given by Fermi's golden rule. Furthermore, Γ_i (usually referred to as *decay width*) depends on the exact process and the relative contribution of each possible decay mode is different. Considering all options for the Higgs, the full decay width Γ is equal to the sum of the individual widths and inversely proportional to the lifetime of the particle. Thus, a fast or slow decay traduces in a respective broadening or narrowing of the events distribution around the pole mass. For the SM Higgs, the predicted width has been determined to be around 5 MeV which is considerably narrower than the W and Z boson cases, with decay widths larger than 2 GeV.

It is illustrative to mention that, even showing low branching ratios (BR), the decay modes that allowed the Higgs discovery in 2012 correspond to $H \to ZZ$ (with each Z decaying leptonically) and $H \to \gamma\gamma$ channels, whose Feynman diagrams are shown in figure 2.4. This was possible due to ATLAS and CMS capability for distinguishing these final states from the predominant hadronic background at the LHC.

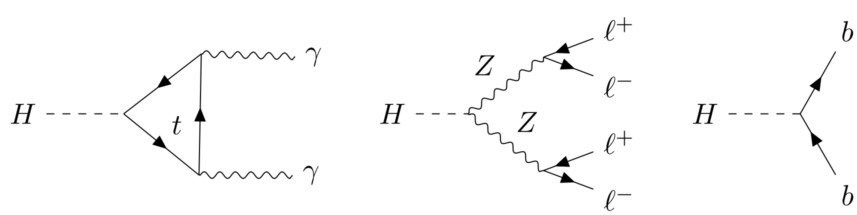

Figure 2.4: 2012 Higgs discovery channels $H \to \gamma\gamma$ and $H \to ZZ \to 4\ell$, plus the decay mode with the larger branching ratio (or BR, given by Γ/Γ_i) $H \to b\bar{b}$. Note that, even if the coupling would be stronger, the decay to a pair of top quarks is kinematically forbidden.

The branching ratios for the SM Higgs and their relative contributions to the width are visible in figure 2.5. At this point, it is crucial to note that not all predicted decay modes for the Higgs have been observed, where some of them are even expected to leave the detector completely unobserved.

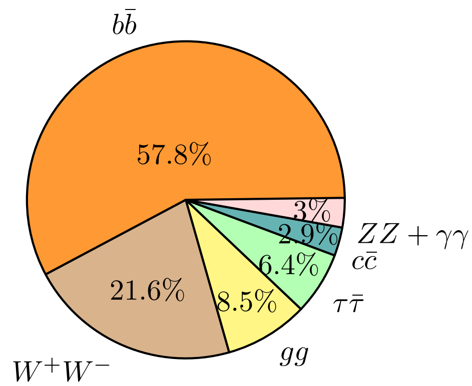

Figure 2.5: Percentage branching ratios for a Higgs boson of mass m_H = 125 GeV. Many EW decay channels, like $\tau\tau$ and ZZ, usually display a high E_T^{miss} signature (related, for example, to final states containing neutrinos).

2.4 Going BSM: Hidden Higgs decays

Even though the Higgs has been observed to decay into different SM channels, including pairs of vector bosons and b quarks, there are constrains on the remaining SM branching ratios and on possible brand new decay modes. In ATLAS, for example, an upper limit on the branching fraction for $H \to$ *invisible* of 11% has been observed at 95% confidence level, using the combined data of the first two runs [35]. With this in mind, a possible scenario predicted by some BSM theories postulates that the Higgs boson could work like a portal to a new, unexplored *dark sector* of particles and interactions that would relate to the Dark Matter (DM) phenomenon.

From the many possibilities postulated during the years, this thesis explores the existence of a light hidden sector weakly coupled to the SM and with a minimal new content of particles, where the hidden lightest stable particle (HLSP) is a candidate for DM. These DM particles may be produced in cascades resulting from Higgs decays, where other unstable hidden mediators could be produced and decay to SM particles in distinguishable ways.

A small review of the theoretical framework of this work is given in section 2.4.1, followed by a characterisation of hidden Higgs decays and their predicted signatures in section 2.4.2.

2.4.1 FRVZ benchmark model

The Falkowski–Ruderman–Volansky–Zupan (FRVZ) model [33; 34], proposed a couple of years before the discovery of the Higgs, explores the existence of a hidden sector with gauge group $U(1)_d$, broken at the GeV scale and weakly interacting with SM particles. Originally imagined to allow for possible ways in which Higgs decays could be hiding in collider experiments, it postulates a minimal number of new particles that would allow for the Higgs to cascade into the hidden sector:

- A massive dark photon γ_d,
- Two dark fermions f_{d_1} and f_{d_2}, where f_{d_2} is heavier and can decay to f_{d_1}, which is the HLSP and thus a DM candidate,
- One hidden scalar h_d, that gives mass to the previous particles.

All masses are assumed to be between 100MeV and a few GeV, and can be arranged in various patterns leading to different final state topologies. For this work, the masses of the dark fermions are chosen to be light relative to the Higgs, and far from the kinematic threshold $m_{LSP} + m_{\gamma_d} = m_{f_{d_2}}$.

In this model, the hidden sector can couple to the SM via two main mechanisms referred to as *portals*. The first one, commonly called Higgs portal, implies the existence of a mix between the SM Higgs and the new dark scalar field;

$$\mathcal{L}_{mix} \propto -\kappa|\phi_{SM}|^2|\phi_d|^2 \tag{2.41}$$

where κ is the mixing parameter that allows the Higgs to effectively decay to a pair of f_{d_2} fermions with a certain BR. These, at the same time, can decay to the HLSP of the theory by emitting dark photons that mix kinetically with the hypercharge field B_μ

$$\mathcal{L}_{mix} \propto \frac{1}{2}\epsilon\gamma_d^{\mu\nu}B_{\mu\nu} = \frac{1}{2}\epsilon\gamma_d^{\mu\nu}(\cos\theta_W A_{\mu\nu} - \sin\theta_W Z_{\mu\nu}) \tag{2.42}$$

where $\gamma_d^{\mu\nu}$ is the field strength tensor of γ_d and ϵ is the mixing parameter, which is small by assumption ($\epsilon \lesssim 10^{-3}$). In this way, the dark photon couples to the electromagnetic current with strength $\epsilon e \cos\theta_W$, allowing effective decays to fermion-antifermion pairs of leptons or hadrons. This receives the name of vector portal, as it connects the hidden sector back to the SM.

Considering both mixing terms, the hypothesised decay looks as in figure 2.6.

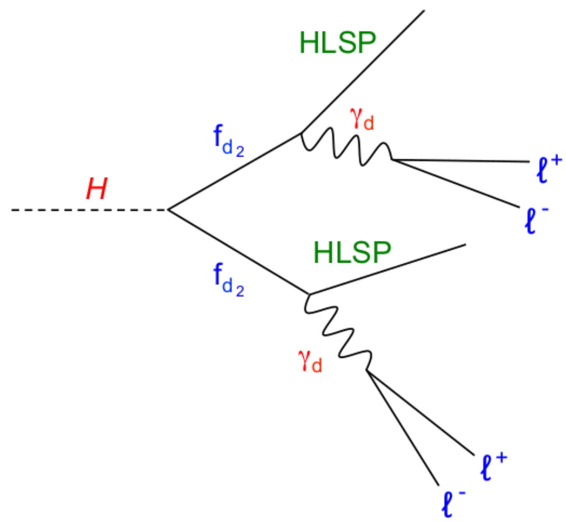

Figure 2.6: FRVZ benchmark decay of the SM Higgs to hidden sector particles, showing final states with leptons or hadrons and DM candidates that would leave the detector unperturbed, expressing as missing energy.

2.4.2 Observables in colliders

Considering that the new sector introduced is rather light compared to the Higgs, the decay kinematics are lead by boosted hidden particles, specially light dark photons decaying to leptons or mesons which later transform into collimated groups of particles that receive the name of *leptons jets* (LJ) [36; 37; 38], or dark photon jets (DPJ) as we will call them from now on.

Since many DPJ topologies are possible, it is experimentally helpful to characterise these decays by observable features like:

- LJ flavour (electronic, muonic or hadronic),
- Leptonic and hadronic multiplicity,

- γ_d lifetime,
- DPJ p_T and η,
- LJ angular aperture

With the γ_d mean lifetime being a free parameter of the model, long-lived dark photons offer a particularly interesting opportunity to explore. Considering that most SM processes in particle collisions occur promptly (i.e., unstable particles are sufficiently short-lived to decay close enough to the collision point for the decay vertex to be individually identified), displaced vertex signatures are another tool to differentiate putative dark signals from SM backgrounds, even with proper decay lengths in the order of millimeters. In our case, the mean lifetime of the γ_d is related to the kinetic-mixing parameter ϵ and its mass [39] approximately as

$$\tau \propto \left[\frac{10^{-4}}{\epsilon}\right]^2 \left[\frac{100 \text{ MeV}}{m_{\gamma_d}}\right]^2 \tag{2.43}$$

where choosing a sufficiently small ϵ (e.g., $10^{-6} < \epsilon < 10^{-5}$) would assure the presence of macroscopically displaced DPJs, where the predominant jet flavour varies with m_{γ_d} as shown in figure 2.7.

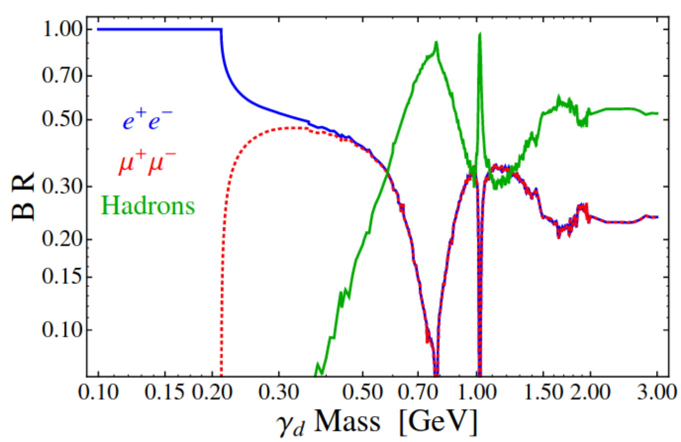

Figure 2.7: Hidden photon branching fractions to electrons, muons and hadrons via the vector portal mechanism and as a function of the dark photon mass [33].

Interesting features are visible immediately. In the $m_{\gamma_d} < 2m_\mu$ region, the only viable decay channel is to electrons while for masses closer to 1 GeV hadronic resonances dominate, offering pure hadronic decays. These different decays are further classified under two experimental categories:

(1) **Muonic DPJs (μDPJ)**, as bundles of collimated muons seen in the muon subdetector system, with no matching tracks or jets in the inner subdetectors.

(2) **Hadronic DPJs (hDPJ)**, as jets with a low electromagnetic energy deposit in the detector (compared to traditional jets), without associated tracks in the most-inner subdetector. Although it may appear misleading, this category also considers electronic DPJs.

A visual depiction of these categories follows in figure 2.8, assuming a layered detector geometry as in modern experiments.

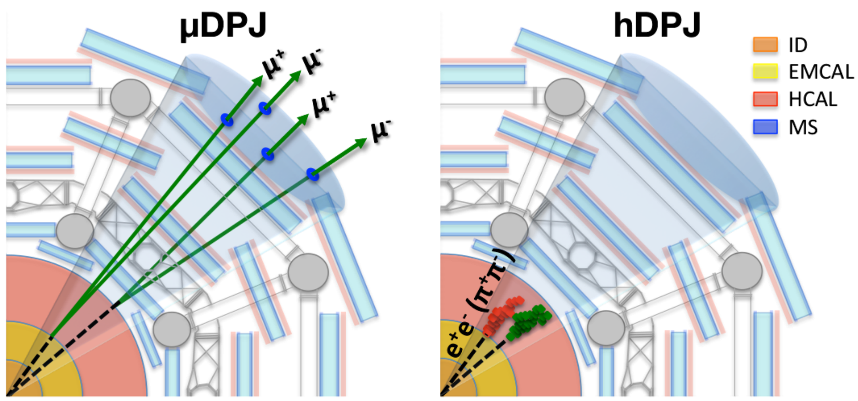

Figure 2.8: The two signatures for reconstructed DPJs: muonic and hadronic.

Many analyses have already searched for prompt and displaced dark photon jet production in several experiments. These constrains are grouped and summarised in figure 2.9, where a large coverage gap is visible for $\epsilon < 10^{-4}$ and masses greater than 100 MeV. To explore this parameter space, this thesis contributes to the search for displaced DPJs coming from Higgs decays as if they were reconstructed using the ATLAS detector, at the Large Hadron Collider. Previous attempts made by the ATLAS collaboration to observe DPJ events are displayed in figure 2.10.

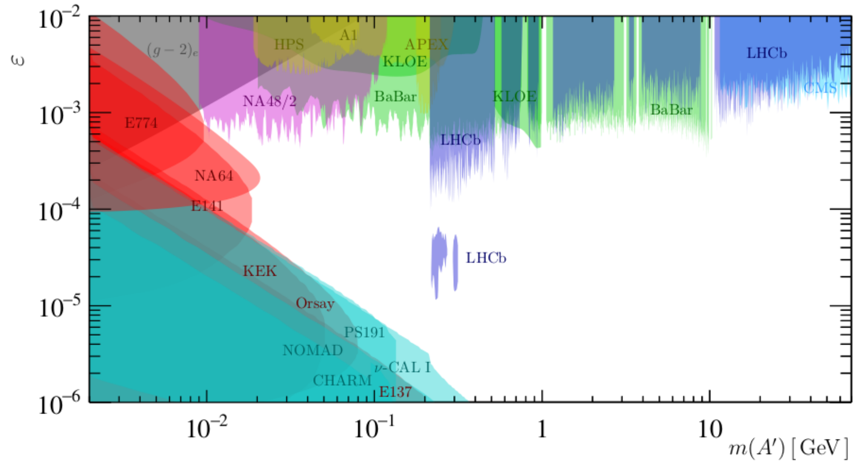

Figure 2.9: Constrains on visible A' decays (analogue to the dark photon) in the ϵ vs $m_{A'}$ plane for: electron beam dump (red), proton beam dump (cyan), electron-positron colliders (green), proton-proton collisions (blue), meson decays (magenta), electron on fixed target experiments (yellow), and muon magnetic moment (grey) [40].

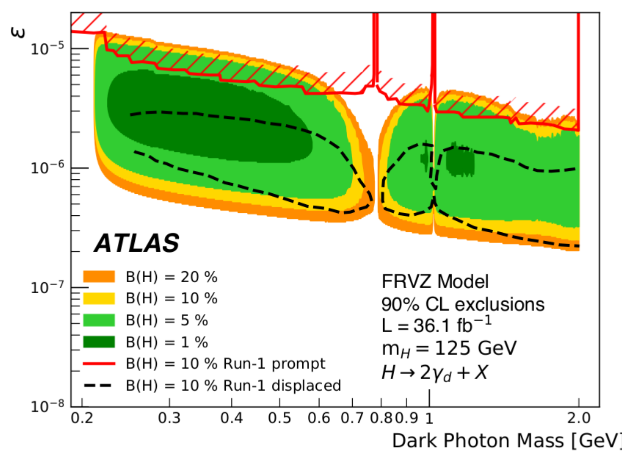

Figure 2.10: Current Run-2 90% confidence level (CL) exclusion contours of the SM Higgs as a function of the γ_d mass and of the kinetic mixing parameter ϵ for the $H \to 2\gamma_d + X$ process. These limits are obtained working in the FRVZ model with branching ratios ranging between 1% and 20%, and considering the next-to-next to leading order (NNLO) gluon-gluon fusion (ggF) cross-section for Higgs production. The plot also shows the limits obtained from the Run-1 ATLAS displaced [41] (black dashed) and prompt [42] (red solid) DP searches.

A detailed description of the collider and the ATLAS detector is presented in the next chapter, leading to the core of analysis in **chapter 4** where a full event selection is designed using FRVZ benchmark simulated events for the second most important Higgs production mode, which has not been explored as of today.

Chapter 3

The LHC and ATLAS

This chapter contextualises the work developed in this thesis by describing the Large Hadron Collider (LHC) and the ATLAS experiment. Sect. 3.1 introduces the properties of the collider, and a full description of the ATLAS detector is given in sect. 3.2.

3.1 The Large Hadron Collider

The LHC [25] is the largest and most powerful particle accelerator on the planet. Proposed officially in 1984, it was built during a ten-year period that finished in 2008 by the European Organization for Nuclear Research (CERN), and it is located under the Swiss-French border close to Geneva.

As a circular proton collider experiment it consists in a 27-kilometre ring carved around 100 metres beneath the surface, equipped with both deflecting and accelerating mechanisms along its circumference, that is initially assisted by a chain of smaller accelerators (as shown in figure 3.1). Within the tunnel, two high-energy beams are accelerated in separate beam pipes and opposite directions by means of rapidly-oscillating electric fields, to energies up to 7 TeV per beam. Each beam is continuously guided around the ring using strong magnetic fields that are generated by numerous superconducting electromagnets, which have to be cooled to temperatures around 2 K using a large distribution system of liquid helium. Further magnets are used to collimate the beams and make them collide at four interaction points (IP) around the ring, where the main four particle detectors are located:

ATLAS, CMS, ALICE and LHCb. The latter is described in the following section.

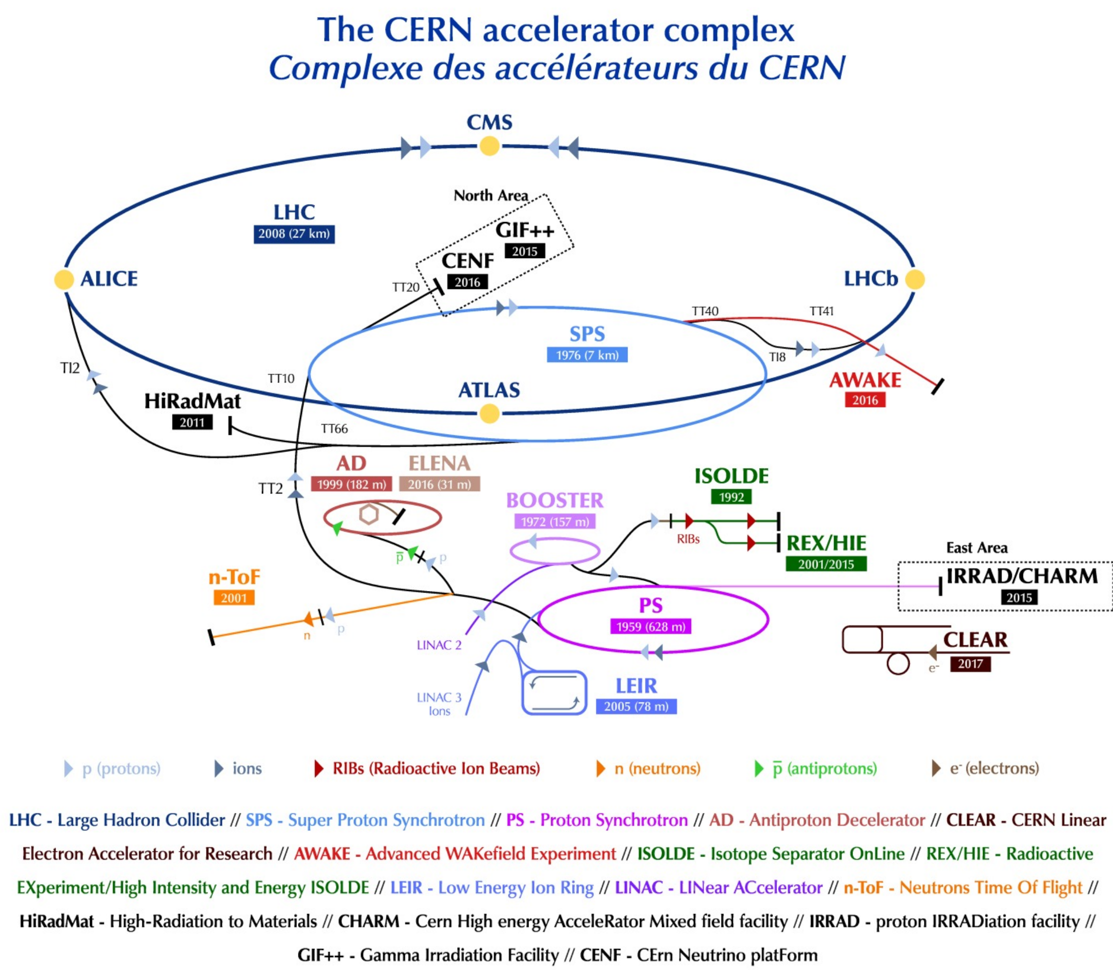

Figure 3.1: The LHC accelerator complex, showing the set of smaller accelerators that prepare the beams before entering the LHC ring, where they later collide in the positions of the four largest experiments [26].

3.2 The ATLAS detector

The ATLAS experiment is a multi-purpose particle detector with forward-backward symmetry, cylindrical geometry and almost full solid angle coverage, that is placed in one of the four interaction points (IP) of the LHC ring. Around 45 metres long and 25 metres high, it is constructed as a series of layers around the beam pipes where specialised sub-detectors and magnets are placed to allow measurements of the trajectory and momenta of particles originated in the collisions.

A diagram of the full detector is shown in figure 3.2, and a description of its components and structure follows through the rest of this chapter.

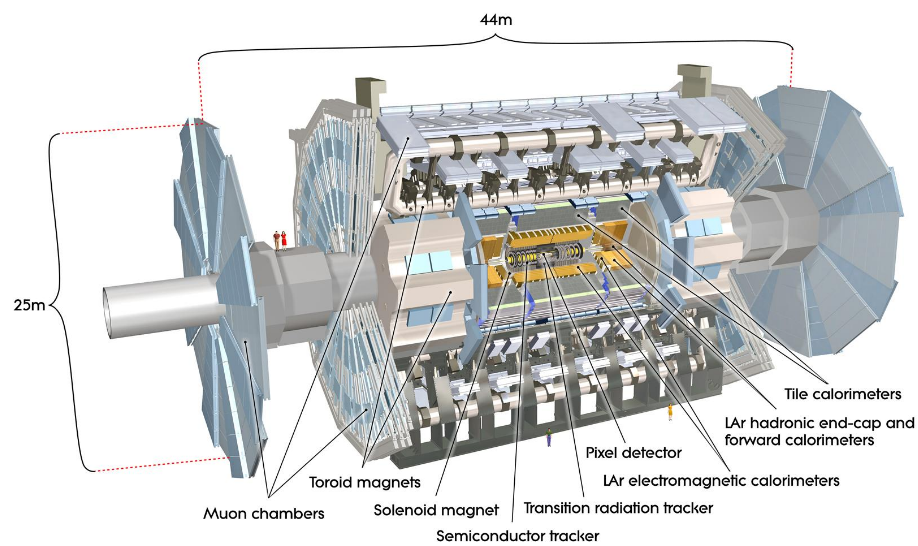

Figure 3.2: Diagram of the ATLAS detector and its components, showing its size in comparison with humans [27].

3.2.1 Coordinate system

In order to standardise all particles measurements, a coordinate system for the detector is chosen with its origin located at the IP. In cartesian coordinates, the x-axis points to the center of the ring, the y-axis to the sky, and the z-axis is tangent to the circumference. In spherical coordinates, ϕ corresponds to the angle in the $x - y$ plane between the x-axis and the projection of the particle's momentum over the transverse plane; while θ is the angle defined in the $r - z$ plane between the z-axis and the momentum vector. A diagram is shown in figure 3.3.

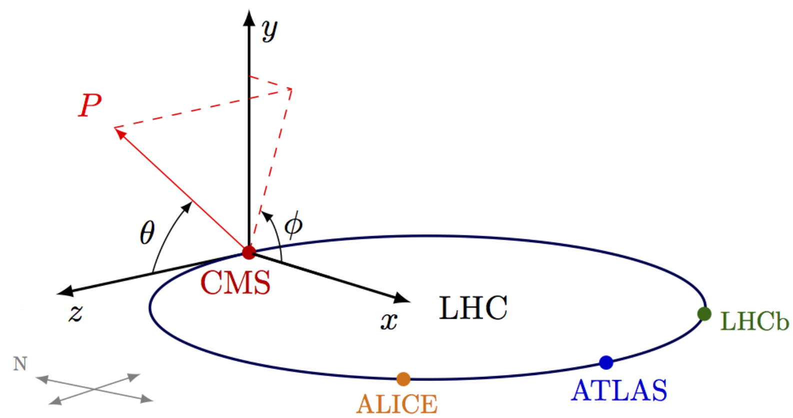

Figure 3.3: Schematic drawing of the detector coordinate system using the CMS experiment as origin. For ATLAS, the system is rotated while keeping the x axis pointing towards the center of the ring [28].

At this point is useful to introduce additional observables commonly used in collider physics. For example, the θ angle is used to define pseudorapidity as $\eta = -\ln\left[\tan\left(\theta/2\right)\right]$ which quantifies the longitudinal angle measured between the y axis and the momentum's projection over the $y - z$ plane. From the definition, $\eta = 0$ for $\theta = \pi/2$ (perpendicular to the beam) and it diverges as $\theta \to 0$ (parallel to the beam). θ is also used to define observables projected over the $x - y$ plane and therefore labelled as *transverse*, such as transverse momentum p_T, given by $p_T = \sqrt{p_x^2 + p_y^2} = |\vec{p}| \sin\theta$; a large η implies a small p_T, and viceversa.

3.2.2 Superconducting magnets

The ATLAS magnet system generates magnetic fields over 4T in magnitude to bend particle trajectories as they propagate, causing most tracks to stay inside the detector and allowing to measure their momenta. It is composed of three main sections which are the Barrel Toroid, the End-cap Toroid and the Central Solenoid, all of them being cooled down to temperatures around 4.5 K.

Each component of the ATLAS magnet system is drawn in figure 3.2 and can be further depicted in figure 3.4.

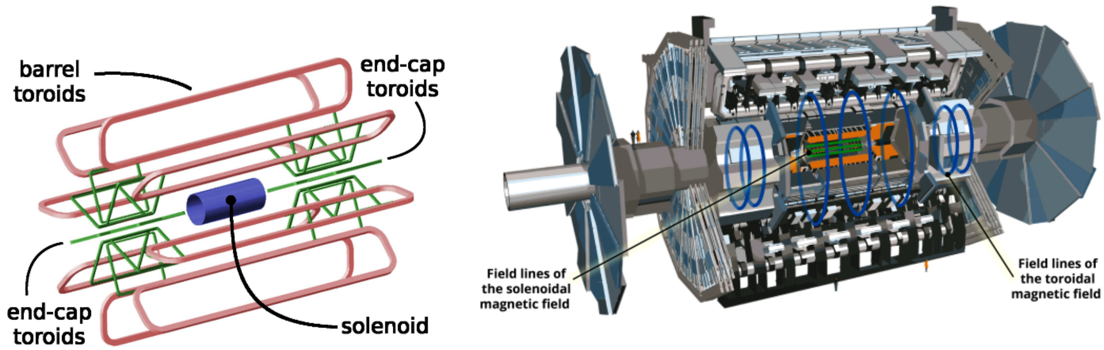

Figure 3.4: Spatial distribution of the ATLAS magnet system and a sketch of the generated field lines [29][30].

3.2.3 Inner Detector

The Inner Detector (ID) is the inner most part of the ATLAS detector, and it provides the first and most sensitive measurement of particles tracks and momenta using silicon detectors and radiation emitted when particles change media. It is formed by a Pixel Detector and a microstrip Semiconductor Tracker (SCT), both made of silicon. Also, it is surrounded by a Transition Radiation Tracker (TRT) formed by a large cylindrical web of thin straw tubes whose material emits light when a charged particle passes through. This light is then used to track the paths of the particles in the 2T axial magnetic field generated by the solenoid magnet, allowing to measure their charge and momentum.

The dimensions and more details about the ID can be seen in figure 3.5.

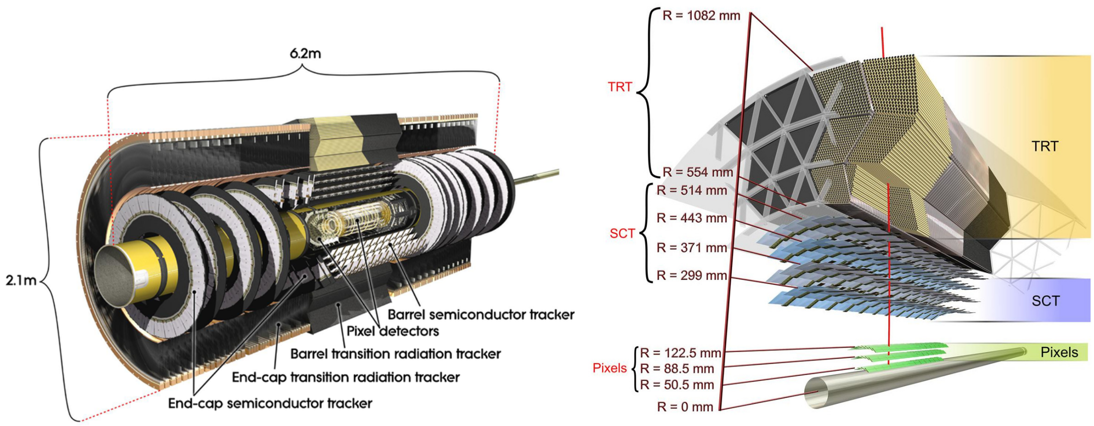

Figure 3.5: Longitudinal (left) and transverse (right) sections of the ID. The outer straw tubes, forming the TRT, also offer a way to distinguish lighter and heavier particles (like electrons from pions), since the amount of energy radiated by a particle when changing media is inversely proportional to a power of its mass [27].

3.2.4 Calorimeters

The Calorimeter system uses highly-stopping materials to slow down most of the particles coming from the collisions and measure the energy deposited in the detector. There are two kinds: electromagnetic (EM; for stopping electrons and photons as they interact with matter) and hadronic calorimeters (for hadrons interacting with atomic nuclei).
Its components are the Liquid Argon (LAr) Calorimeter and the Tile Hadronic Calorimeter (TileCal). The LAr system works with metallic layers (tungsten, copper or lead) and liquid argon at $-184\,^{\circ}\mathrm{C}$, and consists in a forward calorimeter (situated in the boosted region close around the beam pipe), EM and hadronic end-cap calorimeters, and an EM barrel calorimeter. The TileCal, on its side, extends over the barrel and is made of iron plates (that form wedges) and around $420,000$ plastic scintillator tiles, weighting approximately $30,000$ kilograms.

A representation of calorimeter sections and their spatial distribution inside the detector are shown in figure 3.6.

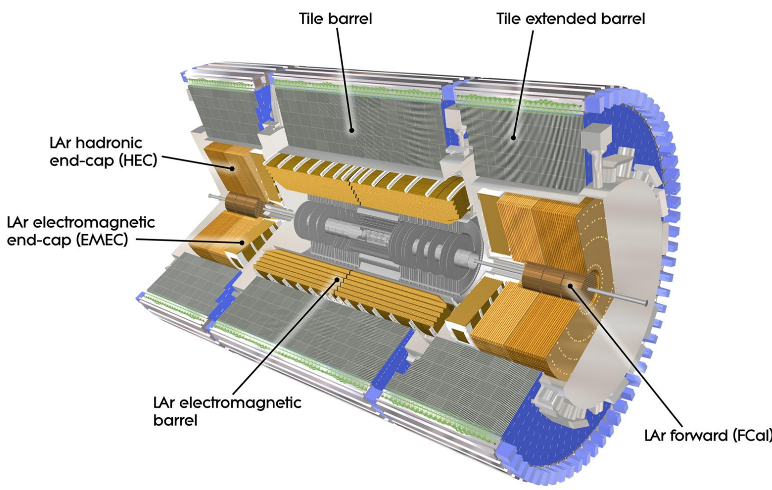

Figure 3.6: Digital illustration of the ATLAS LAr and Tile calorimeters and their subsections [27].

3.2.5 Muon Spectrometer

As muons interact weakly with matter and most of them cannot be stopped by the previous subdetectors, a full Muon Spectrometer (MS) in the exterior of the detector is needed to measure their charge and momenta providing trigger and precision-tracking systems. For this, it is composed of four main subsections: Cathode Strip Chambers (CSC), Monitored Drift Tubes (MDT), Resistive Plate Chambers (RPC) and Thin Gap Chambers (TGC). The latter two are used for triggering and provide a second coordinate measurement for muons after the ID. This is also accomplished using the CSC system at the end of the detector (close to the beam), while the MDT system is in charge of measuring the curvature of the tracks.

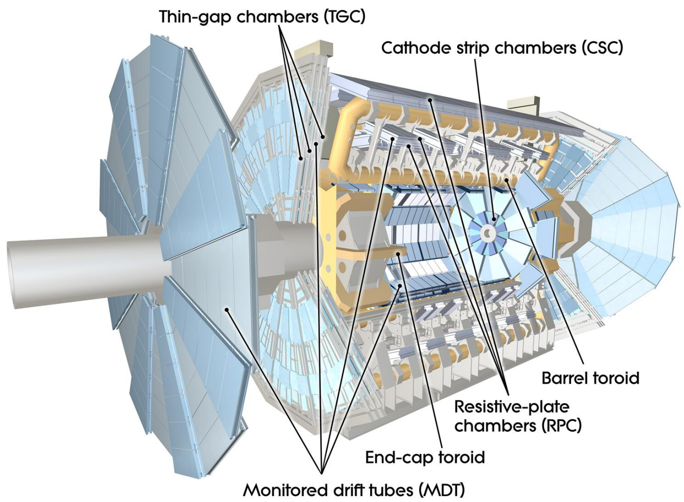

Figure 3.7: Spatial distribution of the MS components [27].

As several upgrades are being developed for Run-3 in many subdetectors and software systems, the MS is getting its inner Small Wheels of chambers upgraded to New Small Wheels (NSWs), consisting in arrays of trapezoidal Small Thin Gap Chambers (sTGC) and Micromega modules (MM) that together aim to provide better trigger and tracking capabilities compared to previous runs, potentially increasing or maintaining the sensitivity of several EW analyses while standing the increased luminosity environment.

3.2.6 Trigger system and data gathering

Since ATLAS can observe up to 1.7 billion *pp* collisions per second ($\sim$ 1 GHz), it uses a layered computing system called Trigger System to select the interesting physics events from all the data, composed of two main levels.

The Level-1 trigger is a hardware-based system that microseconds after the collision decides to keep only physically meaningful events, reducing the detection rate to less than $\sim$ 100 kHz. For this, it uses a subset of information gathered in the calorimeter and muon subdetectors, where events passing the filters are then retrieved from storage buffers to pass to the next level. The High-Level Trigger (HLT) is a software-based system that starts collecting events in readout buffers and, using custom farms of core processor units (CPUs), analyses the events reducing the rate to a maximum of $\sim$ 1000 events per second that are then passed to a data storage system for offline analysis.

A scheme of the Trigger System and its layers is displayed in figure 3.8.

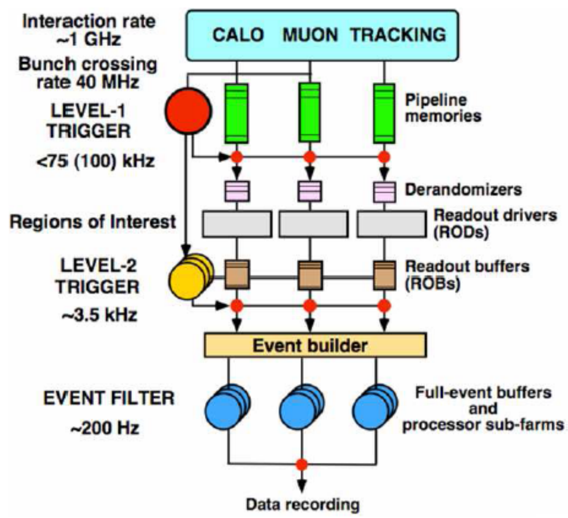

Figure 3.8: Scheme of the ATLAS Trigger System. The all-software HLT is composed of all systems after Level-1 shown in the figure (the Level-2 distinction is no longer used within the collaboration) [31].

Chapter 4

Analysis and results

This chapter is the core of this thesis, which consists on the design of a dedicated event selection for a search of displaced hadronic dark photon jet (hDPJ) signatures in decays of the SM Higgs boson produced via vector boson fusion (VBF) at the LHC. Section 4.1 presents an overview of the analysis, while sections 4.2 to 4.4 give details about the simulated samples, our trigger choice, and the definition of physics objects. Section 4.5 dives into the construction of a full event selection for this search, and section 4.6 closes the chapter by introducing a method to extrapolate signal efficiencies at different dark photon lifetimes for future limits estimation.

4.1 Search overview

While previous DPJ searches have taken place in ATLAS using the gluon-gluon fusion channel, VBF production remains unexplored in the LHC Run-2 data. Considering this mode, the full benchmark signal process for the analysis are shown in figure 4.1.

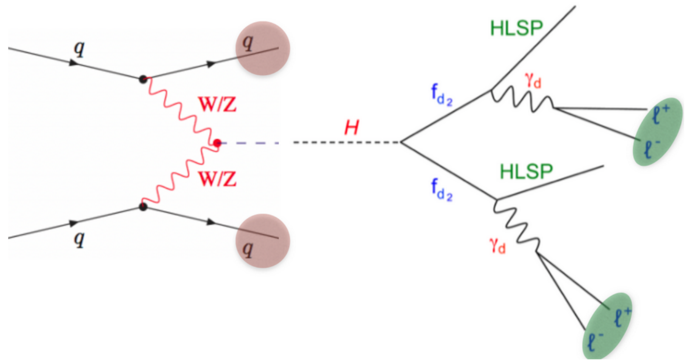

Figure 4.1: Signal diagram showing the FRVZ benchmark hidden Higgs decay discussed in chapter 2 for a Higgs produced via vector boson fusion.

Being the second Higgs production with highest cross section ($\sigma_{VBF}^{13\text{ TeV}} = 3.78$ pb; ggF events being around ten times more), it has a few distinctive signatures that help identify these kind of events:

- Two highly boosted jets with large $\Delta\eta$,
- High dijet invariant mass,
- Small $\Delta\phi$ separation between the jets.

An example for a VBF+E_T^{miss} event at ATLAS is shown in figure 4.2.

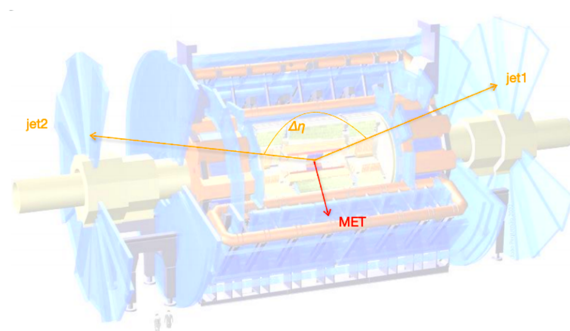

Figure 4.2: Example diagram for a VBF event where the Higgs decay is not observed in the detector and expresses as MET. The two VBF jets are shown in orange, emphasising their large separation in the η plane.

All these special aspects of VBF are crucial to differentiate these events from other SM processes, and will be the starting point for our event selection design in an attempt to

isolate several signal hypotheses from processes with similar final states, commonly known as backgrounds. Here, even when there are no SM processes that can genuinely produce exotic long-lived particles, many processes can fake this experimental signature. From them, the dominant SM background for this search is QCD production of multi-jet events, where high energy jets are produced in the collision and give rise to in-flight decays of kaons and pions that can mimic displaced jets. Similar features are showcased by V+jets events, Top quark production and diboson (WW, WZ, ZZ) events.
Additionally, the interaction of the protons with residual beam gas or beam pipe elements produces another source of reducible background, where high energy muons can be produced near the interaction point and cross the detector horizontally (i.e., parallel to the beam). This source receives the name of beam-induced background (BIB), as these muons can cross the hadronic calorimeter and be reconstructed as hDPJs, and its contribution to the total background is reduced with the help of a specialised neural network tagger.

4.2 Simulated samples

4.2.1 Vector boson fusion FRVZ

Eight different Monte-Carlo (MC) signal samples are used to map distinct regions of the parameter space, where using various γ_d masses allows for different branching fraction ratios. Dark photon's τ remains a free parameter of the model, and values are chosen such that a large volume of the decays occur inside the sensitive ATLAS volume.

All signal samples were generated with the on-the-fly framework `MadGraphControl` to generate Les Houches files [43] in `Athena`, in a specific version that uses the MG5_aMC@NLO v2.2.3 generator [44] for hard-scattering and PYTHIA8 v8.186 for parton-showers and hadronisation [45]. For *pp* collisions, the NNPDF30NLO PDF set is used while for showering the NNPDF23LO set is chosen using the A14 tune. All MC events are processed through the full ATLAS simulation chain based on `GEANT4` [46; 47], to then be reconstructed and processed in the same way as collision data.

The set of generation parameters for the signal sample is listed in table 4.1.

Dataset ID	m_{γ_d} (GeV)	γ_d $c\tau$ (mm)	m_{LSP} (GeV)	$m_{f_{d_2}}$ (GeV)	γ_d decay channel	MC filter eff.
500757	0.1	15	2	5	e^+e^-	0.17425
500758	0.4	50	2	5	$ee, \mu\mu, q\bar{q}$=45%,45%,10%	0.19423
500759	0.4	5	2	5	$ee, \mu\mu, q\bar{q}$=45%,45%,10%	0.19464
500760	0.4	500	2	5	$ee, \mu\mu, q\bar{q}$=45%,45%,10%	0.19528
500761	10	900	10	35	$ee, \mu\mu, q\bar{q}$=40%,40%,20%	0.19528
500762	15	1000	10	45	$ee, \mu\mu, q\bar{q}$=40%,40%,20%	0.20295
500763	10	900	10	35	$q\bar{q}$	0.15555
500764	15	1000	10	45	$q\bar{q}$	0.16963

Table 4.1: VBF FRVZ samples and their parameters. All samples have 160k unweighted (raw) events, and were simulated for a Higgs boson mass of $m_H = 125$ GeV.

4.2.2 SM backgrounds

The main source for background in this analysis are QCD multi-jet events as part of the large hadronic background at the LHC. These events are generated using Pythia v8.235 with the same shower tuning than for signal samples, and are classified in different jet p_T slices based on its truth information.

The second most important background source correspond to V+jets events, simulated by `Sherpa2.2.7` [48] with the NNPDF30NNLO set, and `Herwig7` [49]. These events are produced via strong or electroweak reactions, and some samples are sliced in $p_T(V)$ and m_{jj}. Since these processes resemble our signal the most, they are expected to dominate after event selection.

Other sources of background are diboson events (VV), generated with the same setup as V+jets events, and single-top production plus $t\bar{t}$ events. The latter are generated using `Powheg-BOX` [50] and Pythia8.

Following the same treatment as for signal events, all MC samples go through the simulation of ATLAS detector geometry and responses. This includes effects as multiple pp interactions per bunch crossing (i.e, *pile-up*) and full detector response simulation.

4.3 Trigger for event selection

In the case of searches that involve a Higgs boson, further selection cuts are applied. Since a large fraction of the standard ATLAS triggers [51] are designed assuming particles produced promptly, previous DPJ searches in ATLAS have opted to implement dedicated triggers for displaced searches. For instance, current searches select ggF events by requiring:

- $m_{jj} < 1000$ GeV,
- $E_T^{miss} < 225$ GeV

This forces our search to inverse these cuts and consider them at preselection, as part of a VBF specialised filter, while it simplifies the election of a particular trigger. Due to the missing energy cut, a E_T^{miss} trigger is chosen that combines L1 and HLT information from enriched $W \to \mu\nu$ events where muons are counted as invisible, helping to correct pile-up and calorimeter clustering effects. Here, requiring $E_T^{miss} > 225$ GeV for all events ensures almost a 100% trigger efficiency, as can be seen in figure 4.3. We will use this trigger (or collection of triggers) for event preselection.

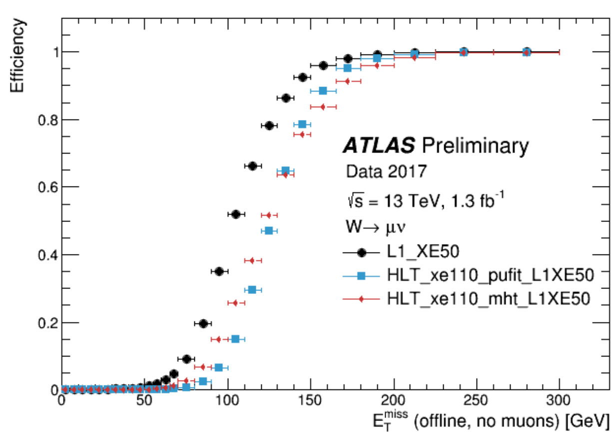

Figure 4.3: Combined L1 and HLT efficiency of the missing transverse energy triggers HLT_xe110_pufit_L1XE50 and HLT_xe110_mht_L1XE50 as well as the efficiency of the corresponding L1 trigger (L1_XE50), as a function of the reconstructed E_T^{miss} (modified to count muons as invisible). The events shown are taken from data with a $W \to \mu\nu$ selection to provide a sample enriched in real E_T^{miss}.

4.4 Object reconstruction

This section defines the criteria for the definition and identification of physics objects for all samples, focusing on dark photon jets of hadronic flavour as our main experimental signature.

4.4.1 Standard jets

A collection of prompt jets is considered to take advantage of the VBF boosted dijet signature while vetoing other modes. Jets are required to have $p_T > 20$ GeV and $|\eta| < 4.9$ and are calibrated and cleaned following the standard ATLAS criteria [52]. For $b-$jets, the MV2c10 algorithm [53] is used, that works with reconstructed charged particle tracks information. A jet is tagged as $b-$jet if the algorithm weight is larger than $\approx 85\%$ the tagging efficiency in $t\bar{t}$ events. In ATLAS, $b-$tagging efficiencies in Run-2 also benefited from the installation of the Insertable B-Layer (IBL) which improved impact parameter resolution and the reconstruction of secondary vertices.
Finally, all jets reconstructing a DPJ (either hadronic or muonic) are removed from these categories.

4.4.2 Missing transverse energy

The missing transverse energy (also known as MET) is reconstructed following the standard ATLAS recommendation including the following E_T^{miss} components: jets, prompt leptons, muons used to reconstruct a DPJ, soft-track terms, and soft-clustering terms. The selection of a MET-based trigger was already described in section 4.3.

4.4.3 Hadronic DPJs

DPJs are classified in μDPJs and hDPJ, as described in section 2.4.2. Since both channels must be targeted with different strategies, we will search for DPJ of the hadronic kind.
Jets from displaced γ_d decays into electron or hadron pairs in the hadronic calorimeter (HCAL) appear narrower than ordinary jets. These are reconstructed from calorimeter

cluster energy deposits using the anti-kt algorithm with a radius parameter of 0.4. Jets are also required to have $p_T \geq 20$ GeV and $|\eta| < 2.5$. The standard ATLAS jet-cleaning criteria and vertex tagging (used in most analyses to reject fake jets) are not applied for dark photon jets since these criteria discard jets with high E_{HCAL}/E_{EMCAL}, a typical discriminant in this kind of searches.

4.5 Event selection for VBF hDPJ

In order to keep putative signal events while rejecting SM backgrounds, several selection cuts are applied to all samples to exploit each possible separation opportunity.

We begin by constructing a set of preselection cuts distinguishing the vector boson fusion channel from the rest, keeping only hadronic dark photon jets, and specially targeting our main multi-jet reducible background. The idea is to set a first level of loose cuts to picture the distribution of different kinematic variables that could be useful for the final selection, building a full set of cuts step by step.

4.5.1 Preselection

Baseline preselection

Our starting point is the signature of the VBF production mode, allowing us to take complete advantage of the boosted dijet kinematics. Three cuts are chosen:

- At least all events must have two jets with $p_T > 30$ GeV.
- The invariant mass of the two leading jets must be $m_{jj} > 1$ TeV.
- An η separation between the leading jets of $|\Delta\eta_{jj}| > 3$.

These are reminiscent of figure 4.2. The m_{jj} results from inverting the cut used in current ggF searches, as mentioned in section 4.3. The shape comparison between production modes motivating this cuts is shown in figure 4.4. We will call these group of cuts our *VBF filter* from here onwards.

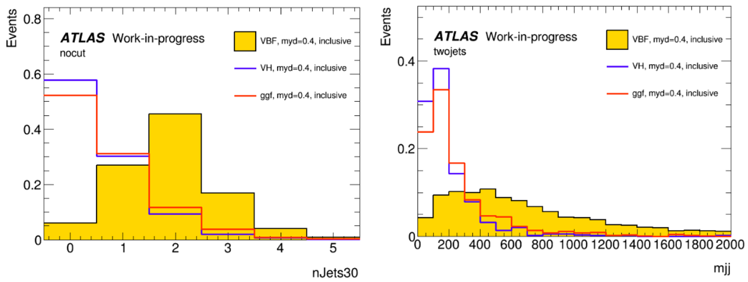

Figure 4.4: Normalised distributions for the VBF filter variables. From left to right, $N_{jets}^{p_T > 30\text{GeV}}$ with no previous cuts applied, and m_{jj} and $|\Delta\eta_{jj}|$ with the two-jet requirement already applied. All distributions are for one signal sample with $m_{\gamma_d} = 0.4$ GeV and inclusive decay channel, and the ggF and VH channels are shown as solid lines.

We proceed with applying the trigger requirement described in section 4.3, where our chain of HLT triggers receives the name of `metTrig`. As previously discussed, an E_T^{miss} cut is also chosen to assure near to 100% trigger efficiency:

- Require all events to pass `metTrig` requirements.
- Additionally, all must display $E_T^{miss} > 225$ GeV.

The missing energy cut also results from inverting the cut mentioned in 4.3, and ensures that our search is fully orthogonal with ggF analyses.

Having identified VBF events that pass all trigger requirements plus the E_T^{miss} cut, we focus on keeping only events from our hypothesised signal where DPJs are hadronic and there are no prompt leptons:

- μDPJ veto; asking for exactly zero muonic DPJs.
- At least one hDPJ in the event.
- No prompt electrons.
- No prompt muons.

All these cuts are not kinetimatically motivated but allow us to recognise signal events using multiplicity observables. The last two cuts listed above are included to reject any event where a Higgs was produced via the VH mechanism and the vector boson decayed leptonically, and thus receives the name of *prompt lepton veto*. At this stage, a quality cut is also introduced to reject lepton jets with a fake low electromagnetic energy deposit, receiving the name of `gapRatio`. These are jets reconstructed in the transition region between the barrel and the end-cap cryostat system, and are removed by requiring the fraction of energy in the tile gap scintillators to be less than 10% (i.e., `gapRatio`> 0.9).

Now that we have exploited VBF signatures and kept only events with DPJs of hadronic flavour, we can search cuts to reduce directly our reducible backgrounds.
We start by targeting top quark production (as well as QCD multi-jet events) by proposing a $b-$jet veto. This requirement helps to reduce single-top and $t\bar{t}$ events where $b-$jets originate from top decays, as visible in figure 4.5. This renders top events as the lowest contribution to the total background at this point, with already less than 1000 weighted events.

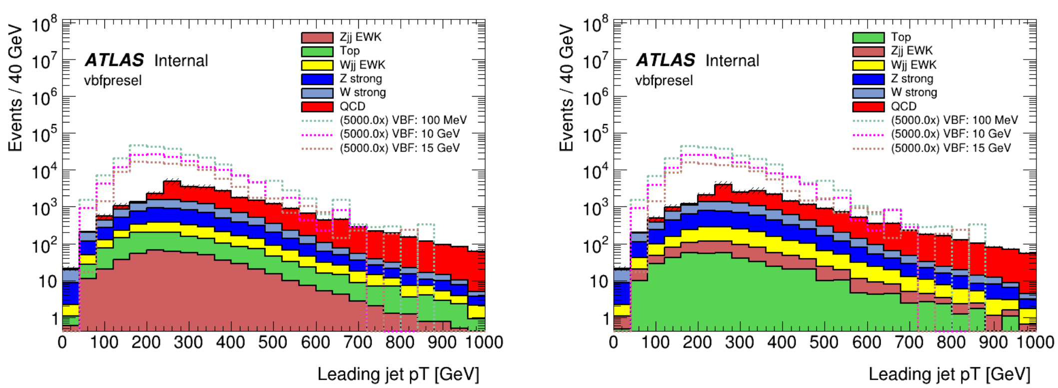

Figure 4.5: Leading jet p_T histograms, shown as example, before (left) and after (right) applying the $b-$jet veto and all previous cuts. All previously mentioned cuts are also applied. After the cut, it is visible that top quark production becomes the process that contributes the less to the stack of backgrounds in the plot. All signal processes (with DSID 500757, 500763 and 500764) are scaled by 5000 to make the dashed lines stand out.

Other variables to discriminate signal from background can be found using normalised distributions to compare shapes between samples. Since our search is highly susceptible to different jet signatures and high missing energy, we can study specialised angular variables relating both observables to find signatures in the background. For lepton jets searches, a useful idea in the past has been to explore the angular distance in the ϕ plane between jets and the direction of the missing energy vector. Two variables of this kind are studied for our search in figure 4.6.

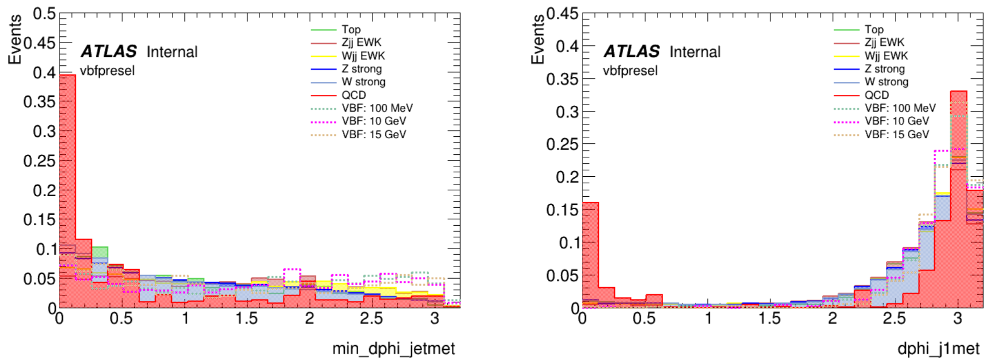

Figure 4.6: Jet-MET angular variables after passing all previous cuts. All processes are normalised by their integrals. The plot on the left shows the minimum ϕ angle between the direction of the total missing energy vector and a jet in the event. The plot on the right shows the same measure but now using the leading jet of the event.

From the `min_dphi_jetmet` distribution we can see that most QCD events have a small minimum jet-MET separation, while for `dphi_j1met` most events show $\Delta\phi \sim \pi$. Taking advantage of this, we initially propose two cuts:

- All events must have `min_dphi_jetmet`> 0.4.
- All events must display `dphi_j1met`> 1.5.

Nonetheless, applying both cuts would be redundant since they are clearly correlated following their definitions. Thus, only the `min_dphi_jetmet` cut will be used since the events targeted by the second cut are already discarded by the first one. The exact correlation for the main background sources can be seen in figure 4.7, as well as the `dphi_j1met` distribution after the `min_dphi_jetmet` cut.

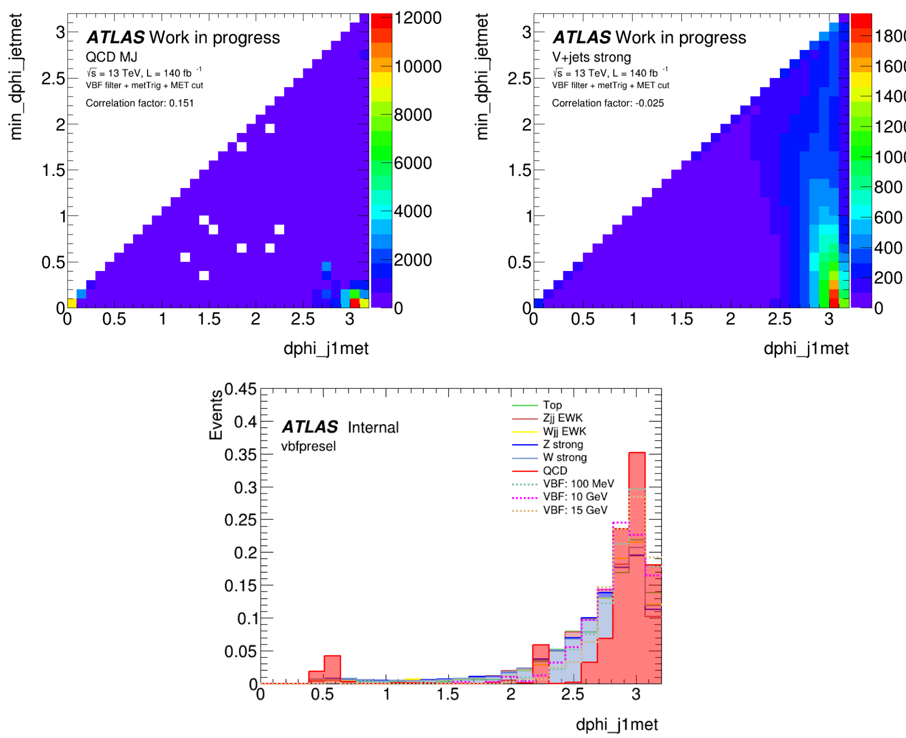

Figure 4.7: Correlation (2D) plots between angular variables for QCD multi-jet and V+jets events, on the top row. The stronger correlation is observed for QCD jets, where most events concentrate at low `min_dphi_jetmet` and high `dphi_j1met`. The lower plot shows the `dphi_j1met` distribution after the `min_dphi_jetmet` requirement, where most events at low $\Delta\phi$ are already rejected.

DPJ-wise selection

Having considered vector boson fusion signatures, hadronic dark photon jets final states, and the rejection of reducible backgrounds, the presence of background events within our signal region is still dominant. Here, to increase the statistical significance of our hypotheses, the information of many observables can be combined to create brand new variables using multi-variate techniques like machine learning (ML) algorithms.

For this search, we use ML discriminants (or *taggers*) previously created by the collaboration based on Convolutional Neural Networks (CNN), where a score between 0 and 1 is individually assigned to each hadronic lepton jet in an event. The taggers receive as input $3D$ representations (including η and ϕ coordinates) of energy deposits in the hadronic calorimeter.

Performing a shape comparison between normalised distributions, two taggers are found to be particularly useful for our search. The Jet Vertex Tagger (`JVT`) attempts to assign jets to the main vertex of the collision, returning a score closer to 1 if this is the likeliest option. This helps mainly to reduce the multi-jet background, since most QCD events obtain a high score. The second tagger, named `DPJtagger`, serves to classify each jet by its degree of resemblance to a true DPJ, with signal scores closer to 1. This tagger will be the most important in our search due to its selection power.
A cut in each respective tagger is proposed:

- Only events with a score of `LJjet1_jvt` < 0.4 are considered.
- Keep only events with a score of `LJjet1_DPJtagger`> 0.5.

The taggers distributions are displayed in figure 4.8, where the `DPJtagger` histogram has the `JVT` requirement already applied to ensure that it is still useful even before the first tagger cut.

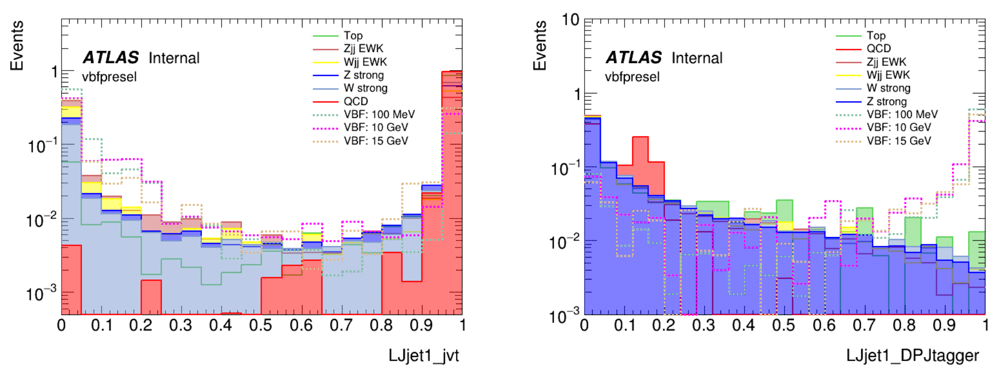

Figure 4.8: `JVT` (left) and `DPJtagger` (right) normalised distributions after all previous cuts. The `DPJ` plot also has the `JVT` cut applied, which traduces on a big reduction on QCD events.

At this stage, the vertex tagger rejects the majority of our background events, with more than 99% of the remaining QCD background eliminated. The second tagger cut is preliminary chosen at 0.5 (and not higher) intentionally, as it will be explored in more detail as the last cut to enter our event selection definition.
For completeness, the correlation between the introduced taggers is studied in figure 4.9 for our main backgrounds, to make explicit any redundancy as we did for the angular jet-MET

variables. In this case, the distribution of events in the $2D$ plane is driven by the fact that signal scores are opposite by design in each tagger (0 for `JVT`, 1 for `DPJtagger`), and there is no reason to remove one of the cuts since both contribute greatly to isolating our signal.

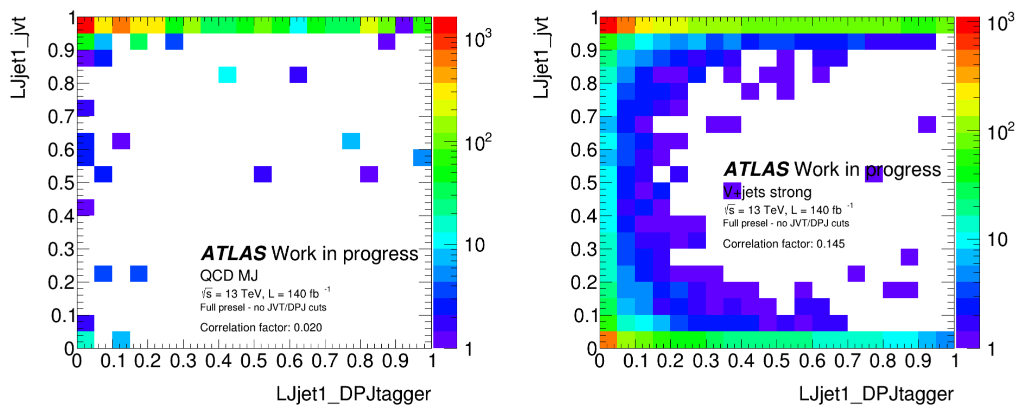

Figure 4.9: Correlation (2D) plots showing the distribution of events in the (`DPJtagger`,`JVT`) plane for QCD multi-jet (left) and strongly produced V+jets (right). As expected, the bulk of QCD events is concentrated at low `DPJtagger` and high `JVT`, while V+jets events are more signal-like.

To complete our preselection, we consider non-collision background sources. As mentioned in section 4.1, BIB events result from interactions between proton bunches and residual beam elements. Since there are no simulated BIB samples or enriched data events for this source, we look directly for BIB traces in 36.1 fb^{-1} of LHC data gathered between 2015 and 2016. Since these events faking the lepton jet signature in the calorimeter are primarily muons that travel horizontally, they tend to cluster at $\phi \approx \pm\pi$. To remove this events, another per-jet tagger was previously developed using the same network architecture than the previous ones, called `BIBtagger`. The optimal tagger cut is chosen to be `BIBtagger`$>$ 0.2 to preserve the signal efficiency and mitigate this background source.

The explicit reduction of BIB events in the mentioned data periods is shown in figure 4.10. The rest of the cuts completing our signal region definition are presented below, starting with a compilation of our selection until this point.

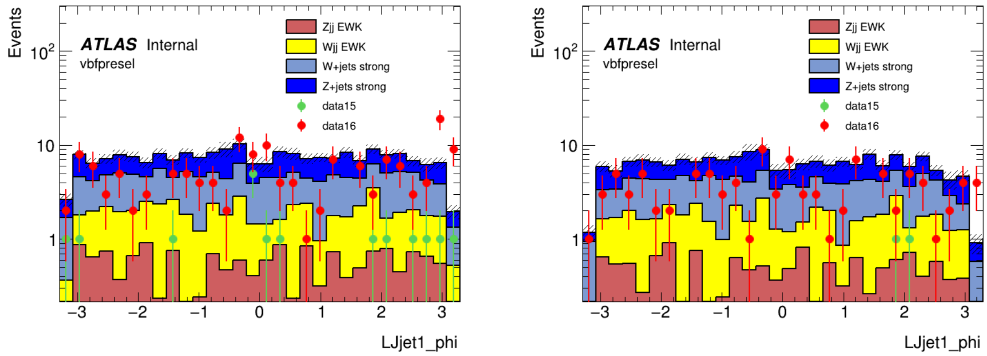

Figure 4.10: Reconstructed lepton jet ϕ distributions before (left) and after (right) applying the `BIBtagger` requirement. Plots show data using red and green markers for the different periods, and all V+jets backgrounds are also displayed, being more than 98% of the background events that survived the selection up this point. While most `data15` events do not survive, the excesses observed in `data16` at $\pm\pi$ are visibly reduced after using the tagger.

4.5.2 Full event selection

Synthesising our set of selections up to now, figure 4.11 shows the cutflow yields for all background processes and the VBF sample ($m_{\gamma_d} = 100$ MeV) with the highest number of events. In this way, the exact effect of each group of preselection cuts is visible for each sample. The final preselection yields are additionally graphed in figure 4.12, to help compare the number of weighted events that survived the selections for each process.

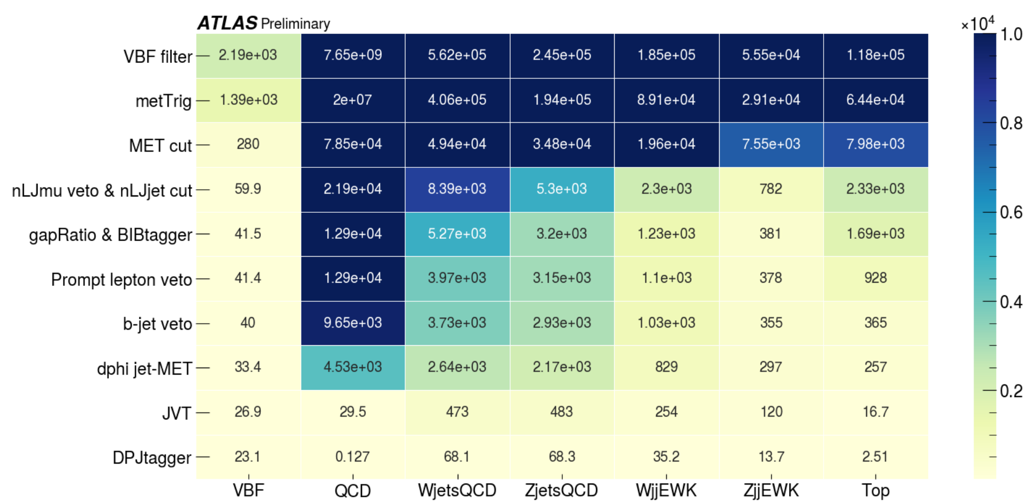

Figure 4.11: Weighted events after preselection for all background processes and one VBF sample ($m_{\gamma_d} = 100$ MeV). A heatmap scale is included to help visualise which backgrounds are bigger, and which are most affected by the selections.

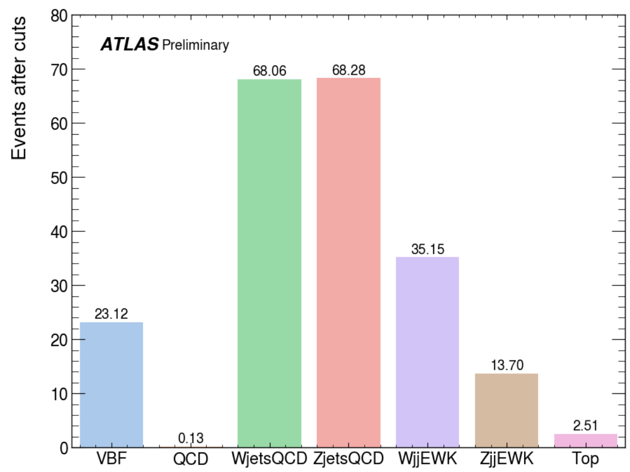

Figure 4.12: Bar plot displaying the final preselection yields, as shown in figure 4.11. For the VBF sample shown, the preselection significance reaches 0.43σ, calculated using the `BinomialExpZ` function from `RooStats` with a 20% fractional uncertainty in the background [54]. Here, it is clear that V+jets events constitute almost all our background after the cuts, with the QCD multi-jet yield not being reliable anymore due to the lack of MC events.

To complete our event selection, two variables are studied in detail: the absolute distance in the ϕ plane between the leading standard jets in the event (i.e., $|\Delta\phi_{jj}|$), and the `DPJtagger` discriminant previously used in preselection. Their weighted distributions can be seen in figure 4.13.

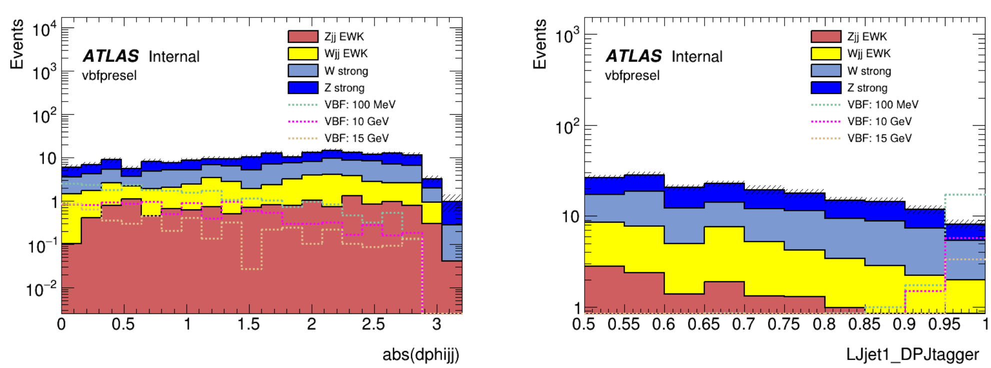

Figure 4.13: $|\Delta\phi_{jj}|$ (left) and `DPJtagger` distributions after all the cuts considered in the preselection. Signal samples are the same as in figure 4.5 but this time are not scaled. V+jets processes are stacked.

Looking at the above histograms, it becomes clear that the best combination of cuts for the two variables would be:

- All events must display $|\Delta\phi_{jj}| < 2.5$.
- All leading lepton jets must have a tagger score above 0.9, with the exact cut to be defined when optimising the significance of the full search.

To find the best `DPJtagger` value, we explore changes in the significance for many cut options between 0.5 (our preselection value) and 1, as represented in figure 4.14.

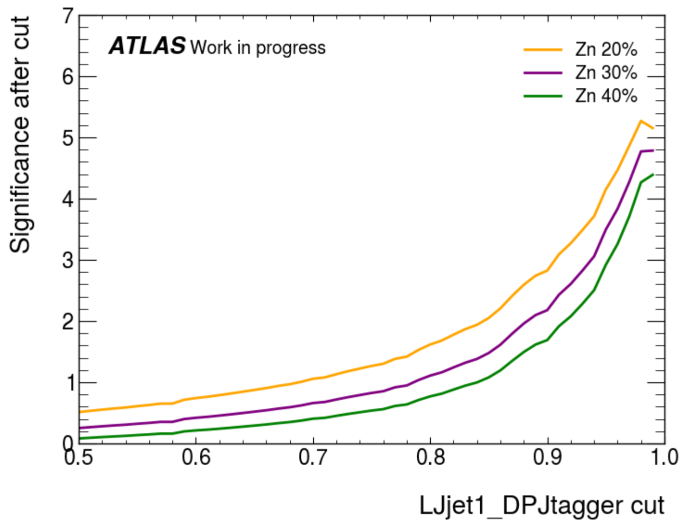

Figure 4.14: Significance optimisation for higher `DPJtagger` cuts, with the $|\Delta\phi_{jj}| < 2.5$ requirement previously applied. Three distinct fractional uncertainties are assumed for the background yield to simulate more realistic significances at different systematic uncertainty scenarios.

From this, we can see that the significance increases as long as the selection gets more aggressive. In this scenario, we cannot simply choose the cut that yields the higher selection significance since a stringer selection would leave all background samples with barely no MC events and unrealistically big uncertainties. To test this directly, a post-preselection cutflow is shown in table 4.2, where the statistical error for each yield is included while increasing the `DPJtagger` cut in steps of 0.01.

Cuts	VBF_100MeV_15mm	Wjets_strong	Zjets_EWK	Top	Zjets_strong	Wjets_EWK	QCD	**Significance**
Preselection	23.1 ± 1.3	68.1 ± 2.9	13.7 ± 1.1	2.5 ± 0.6	68.3 ± 3.1	35.2 ± 2.6	1.3e-01 ± 9.6e-02	0.43σ
abs(dphijj)<2.5	22.4 ± 1.2	56.1 ± 2.7	11.2 ± 1.0	2.2 ± 0.6	55.1 ± 2.4	30.2 ± 2.5	1.3e-01 ± 9.6e-02	0.52σ
LJjet1_DPJtagger>0.9	18.7 ± 1.1	7.1 ± 1.0	6.6e-01 ± 2.5e-01	1.4e-01 ± 1.4e-01	5.6 ± 0.7	2.7 ± 0.7	2.1e-03 ± 2.0e-03	2.85σ
LJjet1_DPJtagger>0.91	18.4 ± 1.1	6.2 ± 0.9	6.4e-01 ± 2.5e-01	1.4e-01 ± 1.4e-01	4.6 ± 0.6	2.1 ± 0.6	2.1e-03 ± 2.0e-03	3.10σ
LJjet1_DPJtagger>0.92	18.1 ± 1.1	5.3 ± 0.8	6.0e-01 ± 2.5e-01	1.4e-01 ± 1.4e-01	4.1 ± 0.5	1.9 ± 0.6	2.1e-03 ± 2.0e-03	3.28σ
LJjet1_DPJtagger>0.93	17.6 ± 1.1	4.5 ± 0.8	5.6e-01 ± 2.5e-01	1.4e-01 ± 1.4e-01	3.1 ± 0.4	1.9 ± 0.6	2.1e-03 ± 2.0e-03	3.50σ
LJjet1_DPJtagger>0.94	17.2 ± 1.1	3.7 ± 0.7	5.4e-01 ± 2.5e-01	1.4e-01 ± 1.4e-01	2.4 ± 0.4	1.8 ± 0.5	2.1e-03 ± 2.0e-03	3.74σ
LJjet1_DPJtagger>0.95	17.0 ± 1.1	2.9 ± 0.6	2.3e-01 ± 1.0e-01	1.4e-01 ± 1.4e-01	2.0 ± 0.4	1.3 ± 0.4	2.1e-03 ± 2.0e-03	4.20σ
LJjet1_DPJtagger>0.96	16.3 ± 1.0	2.1 ± 0.5	2.0e-01 ± 9.7e-02	1.4e-01 ± 1.4e-01	1.5 ± 0.3	1.2 ± 0.4	2.1e-03 ± 2.0e-03	4.52σ
LJjet1_DPJtagger>0.97	15.5 ± 1.0	1.4 ± 0.4	1.3e-01 ± 8.1e-02	1.4e-01 ± 1.4e-01	1.1 ± 0.3	8.8e-01 ± 3.0e-01	2.1e-03 ± 2.0e-03	**X**
LJjet1_DPJtagger>0.98	13.6 ± 1.0	9.3e-01 ± 3.5e-01	8.4e-02 ± 7.6e-02	1.4e-01 ± 1.4e-01	6.2e-01 ± 1.5e-01	4.4e-01 ± 1.9e-01	2.0e-03 ± 2.0e-03	**X**

Table 4.2: Cutflow table exploring the statistical uncertainties in the background yields while increasing the tagger cut. For the last two cuts, no significance is calculated since the error size for each number of background events is equal or greater than 30% with respect to the central value. The significance in the last column is calculated using the `BinomialExpZ` estimation from the `RooStats` package [54], considering only V+jets processes for the total background and with a fractional uncertainty of 20%.

From the table, we observe that a statistical significance close to 3σ is reached with a tagger cut over `DPJtagger`> 0.9, but from this cut onwards the Top and Z+jets EWK predictions cannot be trusted since a statistical error bigger than $\sim 30\%$ indicates around 10 MC events left in those samples.

Following the same idea, and since all background events are practically V+jets events at this point, we stop before the strongly produced V+jets events (our two main backgrounds after selections, as seen in figure 4.12) reach this MC statistic limit. Like this, a `DPJtagger`> 0.95 cut is chosen to complete our signal region definition, reaching a signal significance of 4.20σ for the VBF sample with the lightest dark photon mass.

The full results of the designed event selection for VBF hDPJ searches are displayed below as cutflow tables containing each individual cut and process. The significance reached for each VBF FRVZ sample can be seen in table 4.4, where the lower significance achieved corresponds to the sample with the shortest DP lifetime of $\gamma_d \ c\tau = 5$ mm.

Cuts	Wjets_strong	Zjets_EWK	Top	Zjets_strong	Wjets_EWK	QCD
VBF filter	5.8e+05 ± 4.4e+02	5.5e+04 ± 1.3e+02	1.2e+05 ± 1.4e+02	2.4e+05 ± 2.8e+02	1.8e+05 ± 3.1e+02	7.7e+09 ± 3.1e+07
metTrig	4.2e+05 ± 3.4e+02	2.9e+04 ± 8.7e+01	6.4e+04 ± 1.0e+02	1.9e+05 ± 2.3e+02	8.9e+04 ± 1.8e+02	2.0e+07 ± 1.3e+06
MET>225e3	4.9e+04 ± 8.1e+01	7554.2 ± 37.4	7978.7 ± 36.2	3.5e+04 ± 6.6e+01	2.0e+04 ± 5.9e+01	7.9e+04 ± 5.2e+03
nLJmus20==0	4.9e+04 ± 8.0e+01	7554.4 ± 37.4	7977.4 ± 36.2	3.5e+04 ± 6.6e+01	2.0e+04 ± 5.9e+01	7.9e+04 ± 5.2e+03
nLJjets20≥1	8385.2 ± 36.0	782.5 ± 8.0	2334.1 ± 19.6	5296.4 ± 30.0	2302.3 ± 19.7	2.2e+04 ± 2.9e+03
LJjet1_gapRatio>0.9	6434.6 ± 32.2	500.6 ± 6.3	1992.4 ± 18.1	3967.5 ± 27.0	1570.6 ± 15.9	1.7e+04 ± 1.4e+03
LJjet1_BIBtagger>0.2	5272.2 ± 29.7	381.2 ± 5.4	1689.4 ± 16.7	3201.2 ± 24.9	1232.4 ± 14.1	1.3e+04 ± 1.2e+03
neleSignal==0	4682.2 ± 28.2	378.5 ± 5.4	1284.5 ± 14.5	3190.2 ± 24.8	1113.4 ± 13.6	1.3e+04 ± 1.2e+03
nmuSignal==0	3973.3 ± 26.1	377.6 ± 5.4	928.1 ± 12.3	3148.6 ± 24.7	1100.1 ± 13.5	1.3e+04 ± 1.2e+03
hasBjet==0	3731.5 ± 25.4	355.1 ± 5.3	365.2 ± 7.7	2932.6 ± 24.1	1033.5 ± 13.1	9645.7 ± 982.4
min_dphi_jetmet>0.4	2635.3 ± 20.8	297.4 ± 4.9	257.3 ± 6.5	2168.4 ± 20.3	829.4 ± 12.1	4526.3 ± 704.6
LJjet1_jvt<0.4	472.6 ± 8.1	119.8 ± 3.3	16.7 ± 1.7	483.0 ± 7.3	253.7 ± 7.1	29.5 ± 13.9
LJjet1_DPJtagger>0.5	68.1 ± 2.9	13.7 ± 1.1	2.5 ± 0.6	68.3 ± 3.1	35.2 ± 2.6	1.3e-01 ± 9.6e-02
abs(dphijj)<2.5	56.1 ± 2.7	11.2 ± 1.0	2.2 ± 0.6	55.1 ± 2.4	30.2 ± 2.5	1.3e-01 ± 9.6e-02
LJjet1_DPJtagger>0.95	2.9 ± 0.6	2.3e-01 ± 1.0e-01	1.4e-01 ± 1.4e-01	2.0 ± 0.4	1.3 ± 0.4	2.1e-03 ± 2.0e-03

Table 4.3: Final background yields after each selection cut used to define the signal region. The sum of all backgrounds after cuts is equal to 6.57 ± 1.6, with only strongly produced V+jets samples retaining more than ~ 10 MC events left.

Cuts	500762_15GeV_incl	500760_400MeV_500mm	500757_100MeV	500759_400MeV_5mm	500764_15GeV	500758_400MeV_50mm	500763_10GeV	500761_10GeV_incl
VBF filter	2697.9 ± 14.6	2303.2 ± 13.2	2192.1 ± 12.1	2722.1 ± 14.3	1343.0 ± 8.0	2944.4 ± 15.5	1800.0 ± 10.3	2679.1 ± 14.1
metTrig	1581.4 ± 11.3	1687.8 ± 11.3	1386.7 ± 9.7	1516.8 ± 10.7	678.5 ± 5.8	1852.5 ± 12.2	970.6 ± 7.7	1623.2 ± 11.0
MET>225e3	240.2 ± 4.4	374.1 ± 5.3	280.2 ± 4.4	200.7 ± 3.9	87.6 ± 2.1	351.9 ± 5.4	149.0 ± 3.0	275.6 ± 4.5
nLJmus20==0	215.9 ± 4.2	363.1 ± 5.2	275.5 ± 4.4	142.7 ± 3.3	85.0 ± 2.1	297.9 ± 4.9	144.6 ± 3.0	243.1 ± 4.3
nLJjets20≥1	43.6 ± 1.8	45.3 ± 1.8	59.9 ± 2.0	30.0 ± 1.5	23.1 ± 1.1	58.6 ± 2.2	36.2 ± 1.5	49.4 ± 1.9
LJjet1_gapRatio>0.9	35.5 ± 1.7	33.0 ± 1.5	49.2 ± 1.8	24.5 ± 1.4	19.7 ± 1.0	46.7 ± 2.0	30.1 ± 1.3	39.9 ± 1.7
LJjet1_BIBtagger>0.2	26.7 ± 1.4	24.2 ± 1.3	41.5 ± 1.7	12.1 ± 0.9	15.1 ± 0.9	32.7 ± 1.6	24.0 ± 1.2	28.4 ± 1.4
neleSignal==0	26.7 ± 1.4	24.2 ± 1.3	41.4 ± 1.7	12.1 ± 0.9	15.1 ± 0.9	32.7 ± 1.6	24.0 ± 1.2	28.4 ± 1.4
nmuSignal==0	26.7 ± 1.4	24.2 ± 1.3	41.4 ± 1.7	12.1 ± 0.9	15.1 ± 0.9	32.7 ± 1.6	24.0 ± 1.2	28.4 ± 1.4
hasBjet==0	25.2 ± 1.4	23.4 ± 1.3	40.0 ± 1.7	11.6 ± 0.9	13.9 ± 0.8	31.5 ± 1.6	22.7 ± 1.2	27.5 ± 1.4
min_dphi_jetmet>0.4	22.0 ± 1.3	20.8 ± 1.2	33.4 ± 1.5	8.7 ± 0.8	10.5 ± 0.7	26.2 ± 1.5	19.0 ± 1.1	23.5 ± 1.3
LJjet1_jvt<0.4	15.5 ± 1.1	10.9 ± 0.9	26.9 ± 1.4	5.2 ± 0.6	6.1 ± 0.6	19.9 ± 1.3	12.8 ± 0.9	18.4 ± 1.2
LJjet1_DPJtagger>0.5	11.5 ± 0.9	4.4 ± 0.6	23.1 ± 1.3	2.8 ± 0.4	4.9 ± 0.5	15.8 ± 1.2	10.0 ± 0.8	13.8 ± 1.0
abs(dphijj)<2.5	11.1 ± 0.9	4.3 ± 0.6	22.4 ± 1.2	2.8 ± 0.4	4.7 ± 0.5	14.8 ± 1.1	9.5 ± 0.8	13.1 ± 1.0
LJjet1_DPJtagger>0.95	9.3 ± 0.9	2.8 ± 0.4	17.0 ± 1.1	2.1 ± 0.4	3.2 ± 0.4	11.2 ± 1.0	5.4 ± 0.6	9.9 ± 0.8
Significance	2.51σ	0.75σ	4.20σ	0.53σ	0.87σ	2.96σ	1.51σ	2.68σ

Table 4.4: Final signal yields after each event selection cut. Considering the total V+jets yield after the selections, the significance reached for each signal hypothesis is added in the last row, assuming a 20% uncertainty in the background.

4.6 Lifetime reweighting

Having established a complete set of selection cuts to isolate signal samples from the predicted SM backgrounds, each hypothesis offers a certain degree of sensitivity for the search depending on the signal efficiency of the benchmark sample. Defined as the ratio between the number of weighted events that passed the selection and the total number of weighted events before any cut, this efficiency is used to estimate a limit on the dark photon proper decay length, related to the lifetime by a boost depending on the speed of the particle:

$$\lambda_{decay} = \beta c \tau_0 \gamma \tag{4.1}$$

Now, since each sample is generated with a specific τ_{gen} value and it is not feasible to generate MC samples spanning many orders of magnitude in τ_{gen}, we need a way to extrapolate the efficiency to different proper lifetimes using the signal samples available. This is done using a simple lifetime reweighting algorithm that estimates the signal efficiency of a sample at a different lifetime of interest τ_{new} by assigning a new weight to each event, depending on the number of displaced jets associated to a LLP in that particular event. For the i displaced jet in an event, a weight of the form

$$w_i(t) = \frac{\tau_{gen}}{\exp(-t_i/\tau_{gen})} \cdot \frac{\exp(-t_i/\tau_{new})}{\tau_{new}} \tag{4.2}$$

is computed, where the first factor is used to weight the decay to a flat distribution and the second factor is used to reweight to the desired lifetime. The quantity t_i is the proper decay time of the LLP that gives rise to the displaced jet i, and is calculated from the mass and energy of the LLP. In the model considered, all samples are generated with exactly two dark photons, and the weights obtained for each are multiplied together:

$$w_i^{'}(t_1, t_2) = w_i(t_1) \cdot w_i(t_2) \tag{4.3}$$

This weight is calculated in a per-event basis, and is directly multiplied with the old event weight to mimic a lifetime τ_{new}. Thus, the new reweighted efficiency for a sample equals to

$$\epsilon_{new} = \frac{\Sigma_{i=\text{selected}}\, w_i^{\text{old}} \cdot w_i'}{\Sigma_{\text{all}}} \tag{4.4}$$

where the summation in the denominator is over all events in the sample before any cuts or reweighting procedure.

This algorithm to extrapolate efficiencies as a function of the DP proper decay length is implemented for 4 of our 8 signal samples (one per mass point), rendering the curves displayed in figure 4.15.

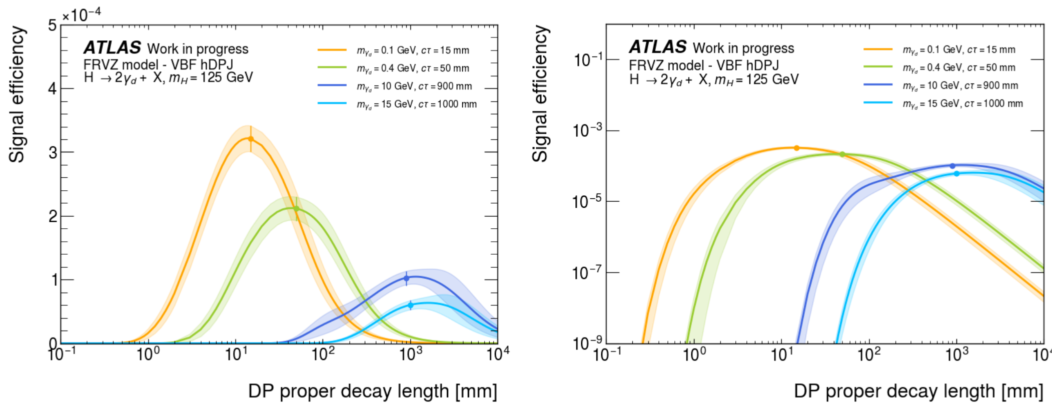

Figure 4.15: Reweighted efficiencies for signal samples with different dark photon mass and τ_{gen} combinations, for dark photon proper decay lengths between 10^{-1} and 10^{4} millimeters. The markers over each curve show the original efficiency after event selection for the respective sample. The plot on the right shows the same information as the left plot but using logarithmic scale in y.

To test the extrapolated efficiencies a validation check is performed between the samples with $m_{\gamma_d} = 0.4$ GeV, comparing the signal efficiencies obtained from the $c\tau = 50$ mm sample with the default (non-reweighted) efficiency of the two benchmark samples with different DP decay lengths. The comparison can be seen in figure 4.16, where the prediction works visibly better when estimating efficiencies at a lower $c\tau$ value than the one used in the reference sample.

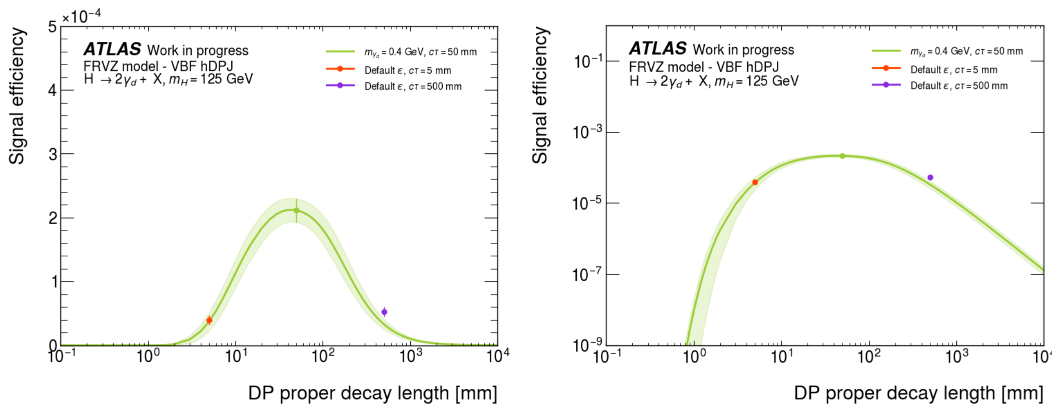

Figure 4.16: Cross-check comparing the efficiencies estimated from the sample with $c\tau = 50$ mm (in green) with the default efficiency of the other two samples generated with the same m_{γ_d} (shown as markers). The plot on the right is equal to the left plot but uses logarithmic scale in the $y-$axis. The validation shows that the reweighting algorithm offers better predictions at $c\tau < c\tau_{gen}$ but fails for any extreme decay length values.

These reweighted efficiencies are the final step to offer a complete working framework for the selection of putative hadronic dark photon jets coming from VBF Higgs decays in ATLAS. With this, each benchmark sample allows for future estimation of limits in the DP proper decay length, contributing to explore the remaining available phase space for dark photon searches in high energy physics.

Chapter 5

Summary and future work

The aim of this thesis has been to search for hadronic dark photon jet (hDPJ) signatures in ATLAS, allegedly produced in Higgs decays coming from vector boson fusion (VBF) events. The main difference with previous searches relies on taking advantage of the well-known VBF signature together with requiring exclusively dark photon jets reconstructed as hadronic.

Using simulated data for various VBF benchmarks and the main respective SM backgrounds, a full event selection was designed to isolate signal events and achieve high statistical significances. This selection considers:

- The dijet kinematic of VBF events, where the two boosted leading jets display high dijet invariant mass and $\Delta\eta$ separation. The $\Delta\phi$ separation between jets is also used.
- A E_T^{miss} trigger with an additional missing energy cut tn ensure full trigger efficiency. This is particularly useful for the search due to production of hidden lightest stable particles (here DM candidates) that express as missing energy.
- Only the hDPJ signature, vetoing all events where muonic DPJs are reconstructed.
- A prompt-lepton veto, to reject events where the Higgs was produced in association with a vector boson that decayed leptonically (i.e., via the VH mechanism).

- A $b-$jet veto, leaving aside all events where a $b-$jet was reconstructed from a top quark decay, either in single-top or $t\bar{t}$ events.
- Angular jet-E_T^{miss} kinematics to recognise features in the main multi-jet background and further reduce it.
- Three specialised tagger variables created using Convolutional Neural Network (CNN) algorithms, looking to use all the possible information to differentiate hDPJs from other jets. This includes information of the reconstructed vertices, jet geometry, calorimeter deposits, among others.

The selection results are summarised in tables 4.3 and 4.4, where a 4.2σ significance was obtained for the VBF benchmark with the lightest dark photon and fully-hadronic decay (m_{γ_d} = 100 Mev, $\gamma_d \rightarrow e^+e^-$), being the signal sample with most events surviving the selection.

Additionally, a lifetime reweighting procedure was implemented to estimate the efficiency (or acceptance, for the designed selection) of most signal samples at dark photon lifetimes different to the one used at generation. The extrapolated efficiencies were validated using three samples simulated with the same m_{γ_d} and different lifetimes, finding mixed agreement depending on the $c\tau$ of the sample used to estimate new efficiencies.

Further studies will follow to assess the best way to estimate signal efficiencies, to later find exclusion limits as a function of the dark photon proper decay length. Other potential studies are contemplated, including data-driven background estimation for sources with not enough Monte Carlo (MC) events after cuts, and a combination with the μDPJ channel after a full selection design. Finally, the results showed in this thesis are going to be contrasted with data recorded by ATLAS in the full Run-2 period (140 fb^{-1}).

Bibliography

[1] S.L. Glashow, *Partial Symmetries of Weak Interactions*, Nucl. Phys. **22** (1961) 579-588, doi:10.1016/0029-5582(61)90469-2.

[2] S. Weinberg, *A Model of Leptons*, Phys. Rev. Lett. **19** (1967) 1264-1266, doi:10.1103/PhysRevLett.19.1264.

[3] J. Goldstone, *Field Theories with Superconductor Solutions*, Nuovo Cim. **19** (1961) 154-164, doi:10.1007/BF02812722.

[4] F. Englert and R. Brout, *Broken Symmetry and the Mass of Gauge Vector Mesons*, Phys. Rev. Lett. **13** (1964) 321, doi:10.1103/PhysRevLett.13.321.

[5] P. W. Higgs, *Broken Symmetries and the Masses of Gauge Bosons*, Phys. Rev. Lett. **13** (1964) 508–509, doi:10.1103/PhysRevLett.13.508.

[6] G.S. Guralnik, C.R. Hagen, and T.W.B. Kibble, *Global Conservation Laws and Massless Particles*, Phys. Rev. Lett. **13** (1964) 585–587, doi:10.1103/PhysRevLett.13.585.

[7] N. Cabbibo, *Unitary Symmetry and Leptonic Decays*, Phys. Rev. Lett. **10** (1963) 531–533, doi:10.1103/PhysRevLett.10.531.

[8] M. Kobayashi and T. Maskawa, *CP Violation in the Renormalizable Theory of Weak Interaction*, Prog. Theor. Phys. **49** (1973) 652-657, doi:10.1143/PTP.49.652.

[9] The Standard Model and beyond, http://united-states.cern/physics/standard-model-and-beyond.

[10] H. Fritzsch and M. Gell-Mann, *Current algebra: Quarks and what else?*, Proceedings, 16th International Conference on High-Energy Physics, ICHEP, Batavia, IL, eConf **C720906V2** (1972) 135-165.

[11] H. Fritzsch, M. Gell-Mann and H. Leutwyler, *Advantages of the Color Octet Gluon Picture*, Phys. Lett. **47B** (1973) 365-368, doi:10.1016/0370-2693(73)90625-4.

[12] D.J. Gross and F. Wilczek, *Asymptotically Free Gauge Theories - I*, Phys. Rev. **D8** (1973) 3633-3652, doi:10.1103/PhysRevD.8.3633.

[13] H.D. Politzer, *Reliable Perturbative Results for Strong Interactions?*, Phys. Rev. Lett. **30** (1973) 1346-1349, doi:10.1103/PhysRevLett.30.1346.

[14] M. Gell-Mann, *A Schematic Model of Baryons and Mesons*, Phys. Lett. **8** (1964) 214-215, doi:10.1016/S0031-9163(64)92001-3.

[15] G. Zweig, *An SU(3) model for strong interaction symmetry and its breaking*, Developments in the Quark Theory of Hadrons **1** (1964) 22-101.

[16] A.D. Martin, W.J. Stirling, R.S. Thorne and G. Watt, *Parton distributions for the LHC*, Eur. Phys. J. **C63** (2009) 189-285, doi:10.1140/epjc/s10052-009-1072-5.

[17] J. Goldstone, A. Salam and S. Weinberg, *Broken Symmetries*, Phys. Rev. **127** (1962) 965-970, doi:10.1103/PhysRev.127.965.

[18] T. Nakano and K. Nishijima, *Charge Independence for V-particles*, Prog. Theor. Phys. **10** (1953) 581-582, doi:10.1143/PTP.10.581.

[19] C.S. Wu, E. Ambler, R.W. Hayward, D.D.Hoppes and R.P. Hudson, *Experimental Test of Parity Conservation in Beta Decay*, Phys. Rev. **105** (1957) 1413-1414, doi:10.1103/PhysRev.105.1413.

[20] G. Aad et al., *Observation of a new particle in the search for the Standard Model Higgs boson with the ATLAS detector at the LHC*, Phys. Lett. **B716** (2012) 1-29, doi:10.1016/j.physletb.2012.08.020.

[21] S. Chatrchyan et al., *Observation of a new boson at a mass of 125 GeV with the CMS experiment at the LHC*, Phys. Lett. **B716** (2012) 30-61, doi:10.1016/j.physletb.2012.08.021.

[22] G. Aad et al., *Combined Measurement of the Higgs Boson Mass in pp Collisions at $\sqrt{s}$=7 and 8 TeV with the ATLAS and CMS Experiments*, Phys. Rev. Lett. **114** (2015) 191803, doi:10.1103/PhysRevLett.114.191803.

[23] G. Aad et al., *Study of the spin and parity of the Higgs boson in diboson decays with the ATLAS detector*, Eur. Phys. J. **C75** (2015) 476, doi:10.1140/epjc/s10052-015-3685-1, 10.1140/epjc/s10052-016-3934-y.

[24] G. Aad et al., *Measurements of the Higgs boson production and decay rates and constraints on its couplings from a combined ATLAS and CMS analysis of the LHC pp collision data at $\sqrt{s}$=7 and 8 TeV*, JHEP **08** (2016) 045, doi:10.1007/JHEP08(2016)045.

[25] L. Evans and P. Bryant, *LHC Machine*, JINST **3** (2008) S08001, doi:10.1088/1748-0221/3/08/S08001.

[26] The CERN accelerator complex, http://cds.cern.ch/record/2636343?ln=en.

[27] G. Aad et al., *The ATLAS Experiment at the CERN Large Hadron Collider*, JINST **3** (2008) S08003, doi:10.1088/1748-0221/3/08/S08003.

[28] Conventional coordinate system with LHC and other detectors, https://wiki.physik.uzh.ch/cms/latex:example_spherical_coordinates.

[29] Digital drawing of ATLAS magnet system, http://www.jetgoodson.com/images/thesisImages/magnetSystems.png

[30] Digital illustration of the ATLAS magnet system, https://atlas.cern/discover/detector/magnet-system

[31] Overview of the ATLAS trigger/DAQ system, http://hep.ps.uci.edu/ wclhc07/ATLAS%20TDAQ.pdf

[32] R. Brun and F. Rademakers, *ROOT - An Object Oriented Data Analysis Framework*, Nucl. Inst. & Meth. in Phys. Res. A **389** (1997) 81-86. See also http://root.cern.ch/.

[33] A. F. et al., *Hidden Higgs decaying to lepton jets*, JHEP **04** (2010) p.077, doi:10.1007/JHEP05(2010)077.

[34] A. F. et al., *Discovering Higgs Boson Decays to Lepton Jets at Hadron Colliders*, Phys. Rev. Lett. **105** (2010) p.241801, doi:10.1103/PhysRevLett.105.241801.

[35] ATLAS Collaboration, *Combination of searches for invisible Higgs boson decays with the ATLAS experiment*, (2020) , URL:https://cds.cern.ch/record/2743055.

[36] N. Arkani-Hamed and N. Weiner, *LHC Signals for a SuperUnified Theory of Dark Matter*, JHEP **0812** (2008) p.104, arXiv:0810.0714 [hep-ph].

[37] C. Cheung, J. T. Ruderman, L. T. Wang and I. Yavin, *Lepton Jets in (Supersymmetric) Electroweak Processes*, (2010), arXiv:0909.0290 [hep-ph].

[38] M. Baumgart, C. Cheung, J. T. Ruderman, L. Wang and I. Yavin, *Non-Abelian Dark Sectors and Their Collider Signatures*, JHEP **0904** (2009) p.014, arXiv:0901.0283 [hep-ph].

[39] C. C. et al, *Kinetic mixing as the origin of a light dark-gauge-group scale*, Phys. Rev. D **80** (2009) p.035008, doi:10.1103/PhysRevD.80.035008.

[40] P. I. et al, *Serendipity in dark photon searches*, JHEP **06** (2018) p.004, doi:10.1007/JHEP06(2018)004.

[41] ATLAS Collaboration, *Search for long-lived neutral particles decaying into lepton jets in proton–proton collisions at $\sqrt{s} = 8$ TeV with the ATLAS detector*, JHEP **11** (2014) p.088, doi:10.1007/JHEP11(2014)088.

[42] ATLAS Collaboration, *A search for prompt lepton-jets in pp collisions at $\sqrt{s} = 8$ TeV with the ATLAS detector*, JHEP **02** (2016) p.062, doi:10.1007/JHEP02(2016)062.

[43] J. A. et al, *A standard format for Les Houches Event Files*, Comput. Phys. Commun. **176** (2007) p.300-304, DOI:10.1016/j.cpc.2006.11.010.

[44] J. A. et al, *The automated computation of tree-level and next-to-leading order differential cross sections, and their matching to parton shower simulations*, JHEP **07** (2014) p.079, DOI:10.1007/JHEP07(2014)079.

[45] T. Sjöstrand, S. Mrenna, P. Skands, *A Brief Introduction to PYTHIA 8.1*, Comput. Phys. Commun. **178** (2008) p.852-867, DOI:10.1016/j.cpc.2008.01.036.

[46] V. N. Ivanchenko, *Geant4 toolkit for simulation of HEP experiments*, Nucl. Instrum. Meth. **A502** (2003) p.666-668, DOI:10.1016/S0168-9002(03)00538-2.

[47] ATLAS Collaboration, *The ATLAS Simulation Infrastructure*, Eur. Phys. J. **C70** (2010) p.823, DOI:10.1140/epjc/s10052-010-1429-9.

[48] T. G. et al., *Event generation with SHERPA 1.1*, JHEP **02** (2009) p.007, DOI:10.1088/1126-6708/2009/02/007.

[49] M. B. et al., *Herwig++ Physics and Manual*, Eur. Phys. J. **C58** (2008) p.639-707, DOI:10.1140/epjc/s10052-008-0798-9.

[50] S. F. et al., *A positive-weight next-to-leading-order Monte Carlo for heavy flavour hadroproduction*, JHEP **09** (2007) p.126, DOI:10.1088/1126-6708/2007/09/126.

[51] ATLAS Collaboration, *Performance of the ATLAS Trigger System in 2010*, Eur. Phys. J **C72** (2012) p.1849, DOI:10.1140/epjc/s10052-011-1849-1.

[52] ATLAS Collaboration, *Selection of jets produced in 13 TeV proton–proton collisions with the ATLAS detector*, ATLAS-CONF-2015-029 (2015), URL:https://cds.cern.ch/record/2037702.

[53] ATLAS Collaboration, *Commissioning of the ATLAS b-tagging algorithms using $t\bar{t}$ events in early Run-2 data*, ATL-PHYS-PUB-2015-039 (2015), URL:https://cds.cern.ch/record/2047871.

[54] L. M. et al, *The RooStats Project*, PoS (2011), ARXIV:1009.1003v2 [physics.data-an].